Sakai H, et al., Matsumoto N.	Rapid detection of gene mutations responsible for non-syndromic aortic aneurysm and dissection using two different methods: resequencing microarray technology and next-generation sequencing.	Hum Genet	131	591-599	2012
Tsurusaki Y, et al., Matsumoto N.	Mutations affecting components of the SWI/SNF complex cause Coffin-Siris syndrome.	Nat Genet	44(4)	376-378	2012
Saitsu H, et al., Matsumoto N.	Whole exome sequenwcing identifies KCNQ2 mutations in Ohtahara syndrome.	Ann Neurol	72(2)	298-300	2012
Saitsu H, et al., Matsumoto N.	*CASK* aberrations in males with Ohtahara syndrome and cerebellar hypoplasia.	Epilepsia	53(8)	1441-1449	2012
Miyake N, et al., Matsumoto N, et al.	*PAPSS2* mutations cause autosomal recessive brachyolmia.	J Med Genet	49(8)	533-538	2012
Tsurusaki Y, et al., Matsumoto N.	A *DYNC1H1* mutation causes a dominant spinal muscular atrophy with lower extremity predominance.	Neurogenet	13(4)	327-332	2012
Tsurusaki Y, et al., Matsumoto N, Miyake N.	Rapid detection of a mutation causing X-linked leukodystrophy by exome sequencing.	J Med Genet	48 (9)	606-609	2011
Saitsu H, Matsumoto N.	Genetic commentary: *De novo* mutations in epilepsy.	Dev Med Child Neurol	53 (9)	806-807	2011
Tsurusaki Y, et al., Matsumoto N.	Exome sequencing of two patients in a family with atypical X-linked leukodystrophy.	Clin Genet	80 (2)	161-166	2011

Doi H, et al., Matsumoto N	Exome sequencing reveals a homozygous *SYT14* mutation in adult-onset autosomal recessive spinocerebellar ataxia with psychomotor retardation.	Am J Hum Genet	89(2)	320-327	2011
Saitsu H, et al., Matsumoto N.	Mutations in *POLR3A* and *POLR3B* encoding RNA polymerase III subunits cause an autosomal recessive hypomyelinating leukoencephalopathy.	Am J Hum Genet	89(11)	644-651	2011

RESEARCH ARTICLE

Human Mutation

OFFICIAL JOURNAL

HGVS HUMAN GENOME VARIATION SOCIETY

www.hgvs.org

Mitochondrial Complex III Deficiency Caused by a Homozygous *UQCRC2* Mutation Presenting with Neonatal-Onset Recurrent Metabolic Decompensation

Noriko Miyake,[1*†] Shoji Yano,[2†] Chika Sakai,[3] Hideyuki Hatakeyama,[3] Yuichi Matsushima,[3] Masaaki Shiina,[4] Yoriko Watanabe,[5] James Bartley,[6] Jose E. Abdenur,[7] Raymond Y. Wang,[7] Richard Chang,[7] Yoshinori Tsurusaki,[1] Hiroshi Doi,[1] Mitsuko Nakashima,[1] Hirotomo Saitsu,[1] Kazuhiro Ogata,[4] Yu-ichi Goto,[3] and Naomichi Matsumoto[1*]

[1]*Department of Human Genetics, Yokohama City University Graduate School of Medicine, Yokohama, Japan;* [2]*Genetics Division, Department of Pediatrics, LAC+ USC Medical Center, Keck School of Medicine, University of Southern California, Los Angeles, California;* [3]*Department of Mental Retardation and Birth Defect Research, National Institute of Neuroscience, NCNP, Kodaira, Tokyo, Japan;* [4]*Department of Biochemistry, Yokohama City University Graduate School of Medicine, Yokohama, Japan;* [5]*Department of Pediatrics and Child Health, Kurume University School of Medicine, Kurume, Japan;* [6]*Division of Medical Genetics, Department of Pediatrics, Children's Hospital Los Angeles, Los Angeles, California;* [7]*Division of Metabolic Disorders, CHOC Children's, Orange, California*

Communicated by Daniel Nebert

Received 26 June 2012; accepted revised manuscript 7 November 2012.

Published online 19 December 2012 in Wiley Online Library (www.wiley.com/humanmutation). DOI: 10.1002/humu.22257

ABSTRACT: Mitochondrial complex III (CIII) deficiency is a relatively rare disease with high clinical and genetic heterogeneity. CIII comprises 11 subunits encoded by one mitochondrial and 10 nuclear genes. Abnormalities of the nuclear genes such as *BCS1L* and *TTC19* encoding mitochondrial assembly factors are well known, but an explanation of the majority of CIII deficiency remains elusive. Here, we report three patients from a consanguineous Mexican family presenting with neonatal onset of hypoglycemia, lactic acidosis, ketosis, and hyperammonemia. We found a homozygous missense mutation in *UQCRC2* that encodes mitochondrial ubiquinol–cytochrome *c* reductase core protein II by whole-exome sequencing combined with linkage analysis. On the basis of structural modeling, the mutation (p.Arg183Trp) was predicted to destabilize the hydrophobic core at the subunit interface of the core protein II homodimer. In vitro studies using fibroblasts from the index patient clearly indicated CIII deficiency, as well as impaired assembly of the supercomplex formed from complexes I, III, and IV. This is the first described human disease caused by a core protein abnormality in mitochondrial CIII.

Hum Mutat 34:446–452, 2013. © 2012 Wiley Periodicals, Inc.

KEY WORDS: mitochondrial complex III (CIII); UQCRC2; whole exome sequence; supercomplex

Introduction

The mitochondrial respiratory chain generates energy as ATP by means of the electron-transport chain and the oxidative-phosphorylation system. The mitochondrial respiratory chain, located in the inner mitochondrial membrane, is composed of five multimeric protein complexes: I, II, III, IV, and V. Among them, the complex III (CIII) (bc1 complex or ubiquinol–cytochrome *c* reductase; EC1.10.2.2) monomer is composed of 11 proteins [Iwata et al., 1998]. One protein is encoded by mitochondrial DNA (*MTCYB*) and the other 10 are encoded by nuclear DNA. The latter are categorized into three groups: (1) core proteins (encoded by *UQCRC1* and *UQCRC2*), (2) respiratory proteins (*CYC1* and *UQCRFS1*), and (3) low-molecular-weight proteins (*UQCRH*, *UQCRB*, *UQCRQ*, *UCRC*, *UQCR11*, and *UQCRFS1*). In its native state, the CIII monomer is quickly converted into a catalytically active homodimer that is incorporated into a supercomplex (respirasome) with complexes I and IV, and this supercomplex functions as a single enzyme [Schagger and Pfeiffer, 2000].

Mitochondrial CIII enzyme deficiency (CIII deficiency; MIM# 124000) is a relatively rare disease with clinical and genetic heterogeneity. Until now, mutations in four genes have been known to cause autosomal recessive CIII deficiencies: *UQCRB* (NM_006294), *UQCRQ* (NM_014402), *BCS1L* (NM_004328), and *TTC19* (NM_017775). *UQCRB* and *UQCRQ* encode components of CIII itself, whereas *BCS1L* and *TTC19* produce mitochondrial assembly factors. Although recessive *BCS1L* mutations are the most frequent cause of CIII deficiency, the majority of the genetic causes of CIII deficiency remain unknown [Benit et al., 2009; de Lonlay et al.,

Additional Supporting Information may be found in the online version of this article.

[†]These authors contributed equally to this work.

*Correspondence to: Noriko Miyake, Department of Human Genetics, Yokohama City University Graduate School of Medicine, 3-9 Fukuura, Kanazawa-ku, Yokohama 236-0004, Japan. E-mail: Noriko Miyake: nmiyake@yokohama-cu.ac.jp; or Naomichi Matsumoto, Department of Human Genetics, Yokohama City University Graduate School of Medicine, 3-9 Fukuura, Kanazawa-ku, Yokohama 236-0004, Japan. E-mail: naomat@yokohama-cu.ac.jp

Contract grant sponsors: Ministry of Health, Labor, and Welfare; the Japan Science and Technology Agency; the Strategic Research Program for Brain Sciences; Ministry of Education, Culture, Sports, Science, and Technology of Japan; the Japan Society for the Promotion of Science; 2011 Strategic Research Promotion of Yokohama City University; the Japan Epilepsy Research Foundation; and the Takeda Science Foundation.

2001; DiMauro and Schon, 2003; Fernandez-Vizarra et al., 2007; Hinson et al., 2007; Visapaa et al., 2002]. Interestingly, *BCS1L* mutations cause variable clinical presentations: Bjornstad syndrome (MIM# 262000), which is characterized by sensorineural hearing loss and pili torti [Hinson et al., 2007]; GRACILE syndrome (MIM# 603358), which presents with fetal growth retardation, aminoaciduria, cholestasis, iron overload, lactic acidosis, and early death [Visapaa et al., 2002]; and Leigh syndrome (MIM# 256000) [de Lonlay et al., 2001]. A homozygous mutation of *TTC19* causes a progressive neurodegenerative disorder [Ghezzi et al., 2011]. A homozygous 4-bp deletion of *UQCRB* causes hypoglycemia and lactic acidosis [Haut et al., 2003] and a homozygous missense mutation of *UQCRQ* results in severe psychomotor retardation, extrapyramidal signs, and dementia [Barel et al., 2008].

Here, we describe the first human mutation of UQCRC2 encoding core protein 2 of CIII, utilizing linkage analysis and whole-exome sequencing.

Materials and Methods

DNA Preparation

DNAs from family members and fibroblasts from patients were collected after obtaining informed consent. DNA was extracted from blood leukocytes using a QIAamp DNA Blood Midi Kit (Qiagen, Hilden, Germany) or QuickGene-610L (Fujifilm, Tokyo, Japan), according to the manufacturers' instructions. DNAs from 80 Mexican control subjects were purchased from the Coriell Institute for Medical Research (Camden, New Jersey). The experimental protocols were approved by the institutional review board of Yokohama City University.

Linkage Analysis

SNP typing was performed using an Affymetrix Human Mapping SNP 10K Xba I 142 2.0 array (Affymetrix, Santa Clara, California), according to the manufacturer's instructions. A multipoint linkage analysis was performed using Allegro version 2.0 [Gudbjartsson et al., 2005]. An autosomal recessive mode of inheritance with complete penetrance and a disease allele frequency of 0.005 was used.

Exome Sequence

Briefly, 3 μg of genomic DNA was sheared and captured using a NimbleGen SeqCap EZ Exome Library SR (Roche NimbleGen, Inc., Madison, New Jersey), according to the manufacturer's instructions. The captured sample was sequenced on a GAIIx instrument (Illumina, Inc., San Diego, California) using 76-bp paired-end reads. Image analysis and base calling were performed by sequence-control software real-time analysis (Illumina, Inc.) and CASAVA software v1.7 (Illumina, Inc.). The quality-controlled (path-filtered) reads were mapped to human genome reference hg19 with Mapping and Assembly with Qualities (MAQ; http://maq.sourceforge.net/) and NextGENe software v2.00 (SoftGenetics, State College, Pennsylvania). The variants from MAQ were annotated by SeattleSeq annotation 131 (http://snp.gs.washington.edu/SeattleSeqAnnotation131). The priority scheme of the variants was described previously [Tsurusaki et al., 2011]. The nucleotide numbering of the variants reflects the cDNA numbering, with +1 corresponding to the A of the ATG translation initiation codon in the reference sequence, according to journal guidelines (www.hgvs.org/mutnomen). The initiation codon is codon 1.

Expression Vector Preparation

For construction of a mammalian expression vector, full-length *UQCRC2* (NM_003366.2) was amplified from a cDNA library from a multiple-tissue cDNA (MTC) panel (Clontech, Mountain View, California) using KOD-plus DNA polymerase (Toyobo, Osaka, Japan). The PCR product was cloned into the entry vector (pDONR^{TM}221) of the gateway system (Invitrogen, Carlsbad, California). Each of the two missense mutations was independently introduced into the entry clone using a QuickChange II XL site-directed mutagenesis kit (Stratagene, La Jolla, California). Each insert was cloned into pcDNA-DEST40 (C-terminal V5 and 6xHis tag) by LR recombination. All the clones were verified by direct sequencing. In addition, full-length *UQCRC2* (wild type, mutant, or SNP [rs4850: c.548G>A, p.Arg183Gln]) and AcGFP constructs were cloned into multiple cloning sites A and B of the pIRES vector (Clontech).

Intracellular Localization

Each mammalian expression construct (200 ng) was transfected into COS-1 cells using FuGENE6 (Roche Diagnostics, Indianapolis, Indiana). After 24 hr of transfection, MitoTracker Red CMXRos (Invitrogen) was added and incubated for 30 min. The cells were then fixed with 4% paraformaldehyde for 20 min at room temperature. After permeabilization with 0.1% Triton/1× PBS for 10 min, C-terminally V5-6xHis-tagged UQCRC2 protein was stained with a mouse anti-V5 antibody (1:1,000) (Invitrogen) and an Alexa Fluor 488-conjugated goat antimouse IgG secondary antibody (1:1,000) (Molecular Probes, Carlsbad, California). Confocal images were taken with a FLUOVIEW FV1000-D microscope (Olympus, Tokyo, Japan).

Mitochondrial Enzyme Activity Assay

Mitochondrial enzyme activities were measured using a previously reported method [Trounce et al., 1996], with slight modifications. The complex I activity is indicated as the rotenone-sensitive NADH–CoQ1 reductase activity. In control assays, the activity was decreased to 20% by rotenone.

Western Blotting

Mitochondrial enzyme activity and supercomplex formation were analyzed by western blotting. The enzyme activities of the mitochondrial respiratory chain complexes were measured using mitochondrial fractions prepared from primary fibroblasts derived from patient 1 ($n = 3$) and control subjects ($n = 10$). Each measurement was basically performed in triplicate (if the available materials allowed). The values were normalized to complex II or citrate synthase. Immunoblot detection of each respiratory chain complex was performed using mitochondria solubilized with 0.5% *n*-dodecyl-β-D-maltoside (DDM). The same amount of pooled mitochondrial protein from control subjects ($n = 10$) was used as the control. The primary antibodies used were as follows: 2 μg/ml anti-NDUFA9 (complex I; Invitrogen), 0.02 μg/ml anti-SDHA (complex II; Invitrogen), 2 μg/ml anti-UQCRC1 (CIII; Abcam, Cambridge, Massachusetts), 0.2 μg/ml anti-MTCO1 (complex IV; Invitrogen), and

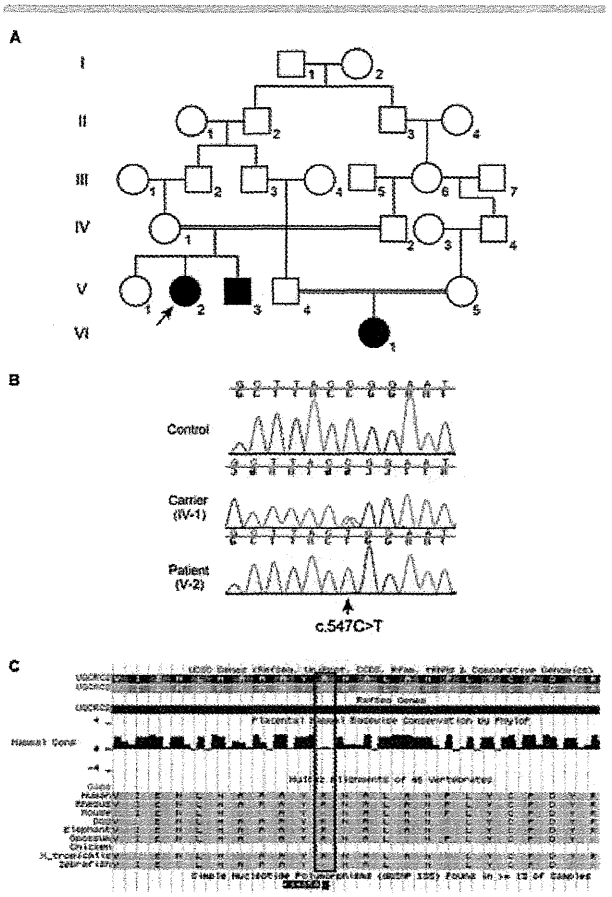

Figure 1. Identification of a *UQCRC2* mutation in a consanguineous Mexican family. **A:** Pedigree of the reported family. The arrow indicates the proband. **B:** Electropherogram of the c.547C>T *UQCRC2* mutation. All three patients (1, 2, and 3) showed a homozygous change, whereas the parents and an unaffected sibling of patients 1 and 2 were heterozygous carriers. The arrow indicates c.547C>T. **C:** Evolutionary conservation of p.Arg183 in UQCRC2 outlined in red. rs4850 (chr 16: 21976762, G>A, p.Arg183Gln) is a common SNP based on the dbSNP135 database.

2 μg/ml anti-ATP5B (complex V; Invitrogen). Immunoblot detection of the respiratory supercomplex was performed using mitochondria solubilized with 1% (w/v) digitonin. The same amount of pooled mitochondrial protein from control subjects (n = 10) was used as the control. The primary antibodies used were as follows: 0.02 μg/ml anti-SDHA (complex II; Invitrogen) and 2 μg/ml anti-UQCRC1 (CIII; Abcam). The band intensity of the supercomplex was estimated by densitometry and normalized to that of complex II. The data were obtained by three independent assays.

Results

Patient 1 (V:2 in Fig. 1A) is a Hispanic female born to a 26-year-old healthy female (G2P2Ab0) and a 28-year-old healthy male who are second cousins. She was delivered at 37 weeks by Cesarean section because of a pathological cardiotocogram. At birth, she weighed 2,329 g (5–10th percentile) with a length of 46 cm (5–10th percentile), and her occipitofrontal circumference was 34 cm (25–50th percentile). Her Apgar scores were 8, 9, and 9 at 1, 5, and 10 min, respectively. She developed a severe metabolic acidosis (pH 7.1, with a base excess of -24.6 mEq/l) within 1 day, requiring admission to a neonatal intensive care unit. Blood lactate and pyruvate on admission were 25.5 mM (reference range: <2.2 mM) and 0.436 mM (reference range: <0.16 mM), respectively (lactate to pyruvate ratio = 58.48). Clinical examination revealed tachypnea (47 breaths/min), tachycardia (181 beats/min), mild subcostal retractions, Levine II/VI systolic cardiac murmur, no organomegaly, and poor sucking reflex. Blood ammonia was 126 μM (reference range in neonates: <80 μM). The patient responded promptly to supportive therapy, with intravenous glucose infusion providing 10 mg/kg/min and a sodium bicarbonate drip improving the blood lactate level down to 12.7 mM within 24 hr. The lactate and pyruvate levels further improved to 3.1 and 0.125 mM within 3 days, respectively. Urine organic acid analysis on admission was remarkable for massive lactic and pyruvic aciduria, as well as ketonuria. Plasma amino acids were remarkable for a high alanine level (1,519 μM; reference range: 200–600 μM). Magnetic resonance imaging (MRI) of the brain revealed small right parietal and temporal infarcts.

She recovered without sequelae and was discharged on full oral feeds with a high-carbohydrate, reduced-fat formula (60% of calories from carbohydrate, 30% of calories from fat) after 1.5 months of hospitalization. She was also diagnosed with an atrial septal defect and renal tubular acidosis. After the initial hospitalization, she was hospitalized more than 10 times because of episodic metabolic decompensation with lactic acidosis (highest value was 10.8 mM at the age of 3 years and 10 months), hyperammonemia (highest value was 346 μM at the age of 3 years and 3 months), ketosis, and hypoglycemia, which were triggered by intercurrent illnesses including fevers, vomiting, and diarrhea. The patient is now 5 years of age, with normal growth and no signs of intellectual disability. The frequency of hospitalization has decreased, although she still requires urgent medical treatment with intravenous glucose infusion to prevent metabolic decompensation during intercurrent illnesses.

Patient 2 (V:3 in Fig. 1A) is a younger full sibling of patient 1. He was born at 39 weeks of gestation by repeat Cesarean section. At birth, he weighed 2,658 g (5–10th percentile) with a length of 49 cm (25–50th percentile), and his occipitofrontal circumference was 34.3 cm (25th percentile). His Apgar scores were 8 and 9 at 1 and 5 min, respectively. He developed tachypnea, grunting, and poor feeding within 1 day because of lactic acidemia. The initial capillary blood gas showed a pH of 7.05, pCO_2 of 25 mmHg, bicarbonate of 5.8 mmol/l, and a base excess of -22 mEq/l. He was intubated for 2 days and treated with intravenous glucose infusion and a bicarbonate drip to correct the metabolic acidosis. Feeding with a high-carbohydrate, reduced-fat formula was started in 10 days. His initial hospitalization was 1-month long, during which he was diagnosed with congenital lactic acidemia and persistent hypoglycemia of unknown etiology. He was treated with corticosteroid replacement therapy owing to adrenal insufficiency for 4 months until a normal adrenocorticotropic hormone stimulation test was obtained. At the age of 8 months, he was found unresponsive after 6 hr of fasting owing to decreased appetite associated with a 2-day mild upper-respiratory-tract infection. At a local emergency room, metabolic acidosis (pH 7.23), hypoglycemia (3 mg/dl; reference range: >60 mg/dl), and hyperammonemia (463 μM), as well as ketosis (blood and urine), were noted. He had five episodes of generalized seizure associated with this episode. Following treatment with levetiracetam, he has been seizure free. Brain MRI findings at the age of 8 months were unremarkable. He was hospitalized for 1 month and discharged without sequelae, and had more than 10 hospitalizations because of similar episodes of lactic acidosis, hypoglycemia, hyperammonemia, and ketosis triggered by intercurrent illnesses. Developmental delay was noted once at 4 months of age. Following

physical and speech therapy, his development was later evaluated as normal at 3 years of age. He is now 4 years of age, with normal growth and no signs of intellectual disability. Physical examination revealed neither dysmorphic features nor abnormal focal neurological signs. He has been fed with a reduced-fat, high-carbohydrate diet and fasting precautions. The frequency of hospitalization has decreased, although he continues to require urgent medical treatment with intravenous glucose infusion to prevent metabolic decompensation during intercurrent illnesses. Laboratory study data obtained in the acute severe metabolic decompensation stage at 16 months of age were remarkable, which are as follows: pH 7.19 capillary blood gas, 11 mg/dl glucose, 348 μM blood ammonia, and 6.8 mM blood lactate. Urine organic acid analysis showed markedly elevated 3-hydroxybutyrate and acetoacetate indicating severe ketosis, markedly elevated lactate and pyruvate indicating lactic acidosis, markedly elevated dicarboxylic acids (adipic acid, 1,194 mmol/mol Cr [reference range: <15 mmol/mol Cr], suberic acid, 122 mmol/mol Cr [reference range: <7 mmol/mol Cr], sebacic acid, 288 mmol/mol Cr [reference range: <2 mmol/mol Cr]) indicating hyperactive fatty acid beta oxidation, and moderately elevated tricarboxylic acid cycle intermediates including malate, fumarate, and 2-oxoglutarate. Plasma amino acids showed elevated alanine at 440 μM (reference range: 23–410 μM). Acylcarnitine profiles obtained at 19 months of age in mild decompensation showed marked elevation of C2 (48 nmol/ml [reference range: 2.6–15.5 nmol/ml]) and moderate elevation of 3-hydroxyacylcarnitines (C12–C18).

Patient 3 (VI:1 in Fig. 1A) is a girl born to consanguineous parents within the same pedigree as patients 1 and 2, but in a different branch. She was small for gestational age and was born vaginally to a 23-year-old mother after a full-term gestation. Her birth weight was 2,200 g. Initially, she had mild respiratory distress and required 1 additional day of monitoring. By 18 months of age, she had undergone four hospitalizations for vomiting, dehydration, and hypoglycemia. An initial blood examination at 18 months of age showed that her blood glucose was 17 mg/dl, bicarbonate was 8 mmol/l, and anion gap was 30 mmol/l. The simultaneous blood lactate and pyruvate levels were 26.3 mg/dl (reference range: <16.0 mg/dl) and 1.5 mg/dl (reference range: <1.5 mg/dl), respectively. She responded quickly to intravenous dextrose with correction of the hypoglycemia and metabolic acidosis. She had developmental delay and microcephaly (second percentile) that led to a brain MRI, but this was interpreted as normal. At 18 months, she spoke only two words but could follow two-part commands. She walked at 15 months of age and had low body weight until starting occupational therapy at 14 months of age. She was not dysmorphic. Her muscle strength and tone were normal when she was in good health, allowing her to climb, hop, and jump in a manner appropriate for her age.

Considering the consanguinity in this family, we hypothesized that the disease was inherited in an autosomal recessive fashion. Linkage analysis using two patients (1 and 2) and three unaffected family members (IV:1, IV:2, and V:1) indicated that homozygous regions totaling 36-Mb were shared by the two affected individuals with logarithm of the odds scores ≥2.0, as calculated by Allegro version 2 [Gudbjartsson et al., 2005] (Supp. Table S1). We then performed whole-exome sequencing of DNA from patient 1. Two homozygous variants within the 36-Mb homozygous regions were identified: c.547C>T, p.Arg183Trp in *UQCRC2* (NM_003366) and c.1675A>G, p.Met559Val in *TNRC6A* (NM_014494). Sanger sequencing confirmed the two variants in patient 1. The Polyphen-2 program (http://genetics.bwh.harvard.edu/pph2/) predicted that p.Arg183Trp in *UQCRC2* and p.Met559Val in *TNRC6A* were probably damaging and benign, respectively (Table 1). *TNRC6A* was ruled out as a candidate because the heterozygous *TNRC6A* change was found in patient 3. *UQCRC2* encodes ubiquinol–cytochrome *c* reductase core protein II (UQCRC2; MIM# 191329), a core protein of CIII. All three patients possessed the homozygous p.Arg183Trp change in *UQCRC2*, whereas the father (IV-2), mother (IV-1), and sister (V-1) (all unaffected) were heterozygous (Fig. 1B). This change was not observed among 80 Mexican control alleles or 750 Japanese control alleles.

Table 1. Prediction of Mutational Effects in UQCRC2

Mutation	Alteration	Type	Grantham score[a]	Polyphen-2	Energy ddG[b]
c.547C>T	p.Arg183Trp	Mutant	101	0.998	10.02
c.548G>A	p.Arg183Gln	SNP	43	0.177	2.19
c.547_548CG>AA	p.Arg183Lys	Ortholog	26	0.001	1.74

[a]Grantham score indicates the chemical dissimilarity caused by codon replacements.
[b]The corrected average interaction energy ddG of each altered amino acid is calculated by FoldX as homozygous mutation.

To predict the effect of the missense mutation (c.547C>T, p.Arg183Trp) on the structural stability of CIII, we calculated the free-energy change of interactions between the core protein monomers (encoded by *UQCRC2*) with and without the mutation using FoldX software (version 3.0) [Guerois et al., 2002; Khan and Vihinen, 2010]. For this calculation, we used the crystal structure of bovine CIII (PDB code 2A06) as a structural model because no crystal structure is available for human UQCRC2. Amino acid position 183 of UQCRC2 is a highly conserved basic amino acid among species from zebrafish to humans (e.g., Arg in humans and cows, Lys in mice; Fig. 1C) and is reported to be substituted for Gln as a nonsynonymous human SNP (rs4850 [c.548G>A, p.Arg183Gln]) (Fig. 1C). Therefore, we also calculated the interaction-energy change upon replacement of Arg183 with Lys or Gln, in addition to the Trp found in the patient. The calculated interaction-energy change caused by replacement of Arg183 with Trp was estimated as 10 kcal/mol, whereas those caused by replacement with Lys or Gln were no more than 2 kcal/mol (Fig. 2A, Table 1). The molecular structure of the wild-type core protein homodimer indicated that the methylene part of the Arg183 side chain of one subunit forms a hydrophobic core with the side chains of His254 and Phe449 of the other subunit at the homodimer interface (Fig. 2B and C). When the Arg183 of the core protein was replaced by Trp, the introduced Trp183 side chain flipped outward from the original side-chain position because of steric hindrance (Fig. 2D). In contrast, when Arg183 was replaced by Lys or Gln, each side chain occupied the original position to maintain a hydrophobic core with the methylene part of Lys or Gln (Fig. 2E and F). This indicates that the Arg183Trp mutation in UQCRC2 would disrupt the hydrophobic core formed at the interface of the UQCRC2-containing complex, resulting in destabilization of CIII. In vitro experiments showing that the exogenous and endogenous expressions of the UQCRC2 mutant were significantly reduced (Supp. Figs. S1 and S2) may support the protein instability.

To test whether this mutation alters UQCRC2 localization at the mitochondrial inner membrane, we created mammalian full-length wild-type, mutant, and SNP (rs4850) constructs; transiently overexpressed them in COS1 cells; and observed their localization microscopically. The mutant protein colocalized with mitochondria, similar to the wild-type and SNP proteins (Supp. Fig. S3). This indicates that the p.Arg183Trp mutation probably does not alter the intracellular localization.

To evaluate mitochondrial function in vitro, we measured the enzyme activities of the mitochondrial respiratory chain complexes

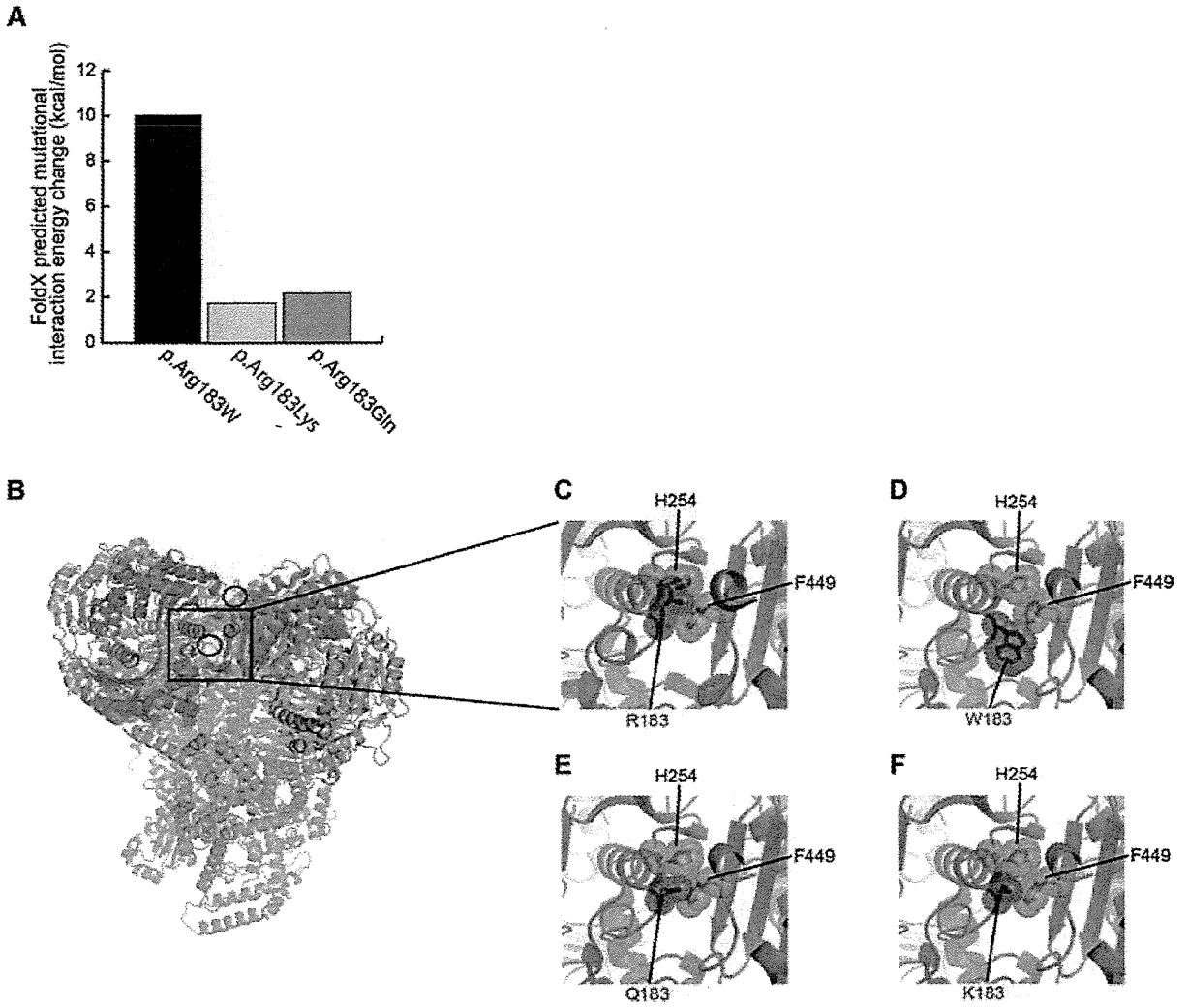

Figure 2. Molecular structural consideration of the effect on dimerization of amino acid replacement at residue position 183 in the core protein. **A:** Calculated interaction-energy change of the core protein homodimer upon replacement by the indicated amino acids at residue 183 using FoldX software. **B:** Overview of the crystal structure of the bovine mitochondrial bc1 (CIII) complex (PDB code 2A06). The core protein monomers are colored green and cyan; the other components are shown in gray. The helices, strands, and loops are shown as ribbons, arrows, and threads, respectively. The red circle indicates residue 183 in the core protein. The box corresponds to the enlarged areas shown in parts (**C**)–(**F**). **C–F:** Detailed views of the core protein homodimerization interface in the wild-type (**C**) and mutated, polymorphic, orthologous (p.Arg183Trp/Gln/Lys) (**D, E, F,** respectively) complex structures. The residues at amino acid 183 of one subunit (red), and His254 and Phe449 of the other subunit (orange) are shown as sticks with Connolly surfaces. All graphics were drawn using PyMOL (www.pymol.com).

using mitochondrial fractions prepared from primary fibroblasts derived from patient 1. With normalization to complex II activity, the CIII activity of patient 1 was decreased to 50% of that in the control subjects (n = 10), whereas complex I activity increased by threefold and complex IV activity remained at the same level as in the control subjects (Fig. 3A). Similar results were obtained using normalization to citrate synthase activity (Fig. 3B). We also investigated the steady-state level of the respiratory complexes by blue-native polyacrylamide gel electrophoresis (BN-PAGE) using the same mitochondrial fraction used for the enzyme activity measurements. For analysis of individual complexes, mitochondria were solubilized with 0.5% (w/v) DDM. For analysis of the supercomplex (complexes I, III, and IV), mitochondria were solubilized with 1% (w/v) digitonin. After BN-PAGE, we performed immunoblotting with specific antibodies for the respiratory complexes (Fig. 3C–F, Supp. Notes, and Supp. Fig. S4). In the patient's fibroblasts, we found that CIII and supercomplex assembly were decreased to 18%–20% $\gg$ 22% –23% (Fig. 3C and D) and 4% $\gg$ 7.5% (Fig. 3E and F) of the levels in pooled control samples, respectively. These data indicate that a homozygous missense mutation (c.547C>T, p.Arg183Trp) in *UQCRC2* causes moderately impaired CIII function and severely decreased amounts of CIII and supercomplex, which would be the primary molecular pathogenesis in the patients.

Discussion

Among the genes known to cause CIII deficiency, impairment of UQCRC2, as found in our patients, leads to a similar clinical course to that reported for UQCRB defects with recurrent crises of

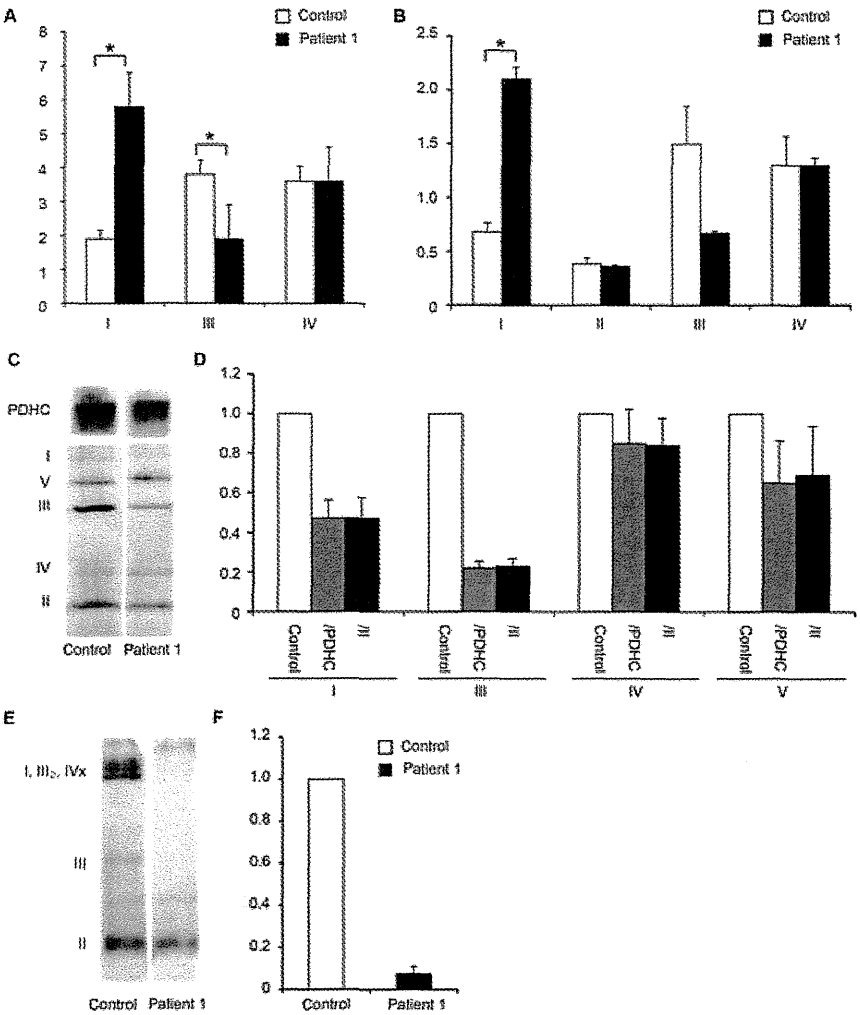

Figure 3. Mitochondrial enzyme activity and supercomplex formation. **A, B:** Enzyme activities of the mitochondrial respiratory chain complexes using mitochondrial fractions prepared from primary fibroblasts derived from patient 1 ($n = 3$) and control subjects ($n = 10$). Each measurement was performed in triplicate. The values were normalized to complex II (**A**) or citrate synthase (**B**). Error bars represent the SEM. **C, D:** Immunoblot detection of each respiratory chain complex using mitochondria solubilized with 0.5% DDM. The same amount of pooled mitochondrial protein from control subjects ($n = 10$) was loaded into the control lane. The band intensity of each respiratory complex was estimated by densitometry and normalized to that of PDHC (gray bar) or complex II (black bar). The data were obtained by three independent assays and the error bars in (**D**) represent the SEM. **E, F:** Immunoblot detection of the respiratory supercomplex using mitochondria solubilized with 1% (w/v) digitonin. The same amount of pooled mitochondrial protein from control subjects ($n = 10$) was loaded into the control lane. The band intensity of the supercomplex was estimated by densitometry and normalized to that of complex II (black bar). The data were obtained by three independent assays and the error bars in (**F**) represent the SEM.

hypoglycemia, lactic acidosis, and ketosis, although the latter did not show hyperammonemia. In contrast, impairment of BCS1L, TTC19, and UQCRQ leads to rather severe complications such as intrauterine growth retardation, liver failure, tubulopathy, sensorineural hearing loss, and abnormalities on brain MRI. The normal development in our patients, despite frequent metabolic crises, may suggest that the UQCRC2 phenotype in our family is milder than disorders of the CIII genes and that this UQCRC2 abnormality does not primarily affect the brain. However, patients 2 and 3 showed epilepsy, and developmental delay was noted in patient 3. It remains to be seen whether this clinical variability is caused by variable expressivity, unknown modifiers, or secondary to the severity of the acute metabolic crises. Interestingly, our patients showed hyperammonemia, highly abnormal urine organic acids indicative of mitochondrial dysfunction, and highly elevated plasma hydroxyl fatty acids during their crises, whereas patients with the other reported CIII impairment disorders did not [Barel et al., 2008; de Lonlay et al., 2001; Ghezzi et al., 2011; Haut et al., 2003; Hinson et al., 2007; Visapaa et al., 2002]. These observations may imply that *UQCRC2* mutations have secondary effects in other metabolic pathways including the Krebs cycle, beta oxidation, and urea cycle.

Conclusion

We have identified, for the first time, a homozygous mutation in human *UQCRC2* encoding a core protein of mitochondrial CIII. Further studies of additional patients with *UQCRC2* abnormalities are necessary to fully understand human CIII disorders.

Acknowledgments

We thank all the family members for participating in this study. We also thank the Commission for Families and Children of Orange County for its support of our clinical work. We appreciate Dr. Takeyori Saheki for useful comments on metabolic decompensation. This study was performed at the Advanced Medical Research Center, Yokohama City University.

Disclosure statement: The authors have no conflict of interest to declare.

References

Barel O, Shorer Z, Flusser H, Ofir R, Narkis G, Finer G, Shalev H, Nasasra A, Saada A, Birk OS. 2008. Mitochondrial complex III deficiency associated with a homozygous mutation in UQCRQ. Am J Hum Genet 82:1211–1216.

Benit P, Lebon S, Rustin P. 2009. Respiratory-chain diseases related to complex III deficiency. Biochim Biophys Acta 1793:181–185.

de Lonlay P, Valnot I, Barrientos A, Gorbatyuk M, Tzagoloff A, Taanman JW, Benayoun E, Chretien D, Kadhom N, Lombes A, de Baulny HO, Niaudet P, et al. 2001. A mutant mitochondrial respiratory chain assembly protein causes complex III deficiency in patients with tubulopathy, encephalopathy and liver failure. Nat Genet 29:57–60.

DiMauro S, Schon EA. 2003. Mitochondrial respiratory-chain diseases. N Engl J Med 348:2656–2668.

Fernandez-Vizarra E, Bugiani M, Goffrini P, Carrara F, Farina L, Procopio E, Donati A, Uziel G, Ferrero I, Zeviani M. 2007. Impaired complex III assembly associated with BCS*1L* gene mutations in isolated mitochondrial encephalopathy. Hum Mol Genet 16:1241–1252.

Ghezzi D, Arzuffi P, Zordan M, Da Re C, Lamperti C, Benna C, D'Adamo P, Diodato D, Costa R, Mariotti C, Uziel G, Smiderle C, et al. 2011. Mutations in TTC*19* cause mitochondrial complex III deficiency and neurological impairment in humans and flies. Nat Genet 43:259–263.

Gudbjartsson DF, Thorvaldsson T, Kong A, Gunnarsson G, Ingolfsdottir A. 2005. Allegro version 2. Nat Genet 37:1015–1016.

Guerois R, Nielsen JE, Serrano L. 2002. Predicting changes in the stability of proteins and protein complexes: a study of more than 1000 mutations. J Mol Biol 320:369–387.

Haut S, Brivet M, Touati G, Rustin P, Lebon S, Garcia-Cazorla A, Saudubray JM, Boutron A, Legrand A, Slama A. 2003. A deletion in the human QP-C gene causes a complex III deficiency resulting in hypoglycaemia and lactic acidosis. Hum Genet 113:118–122.

Hinson JT, Fantin VR, Schonberger J, Breivik N, Siem G, McDonough B, Sharma P, Keogh I, Godinho R, Santos F, Esparza A, Nicolau Y, et al. 2007. Missense mutations in the BCS*1L* gene as a cause of the Bjornstad syndrome. N Engl J Med 356:809–819.

Iwata S, Lee JW, Okada K, Lee JK, Iwata M, Rasmussen B, Link TA, Ramaswamy S, Jap BK. 1998. Complete structure of the 11-subunit bovine mitochondrial cytochrome bc1 complex. Science 281:64–71.

Khan S, Vihinen M. 2010. Performance of protein stability predictors. Hum Mutat 31:675–684.

Mitsuhashi S, Hatakeyama H, Karahashi M, Koumura T, Nonaka I, Hayashi YK, Noguchi S, Sher RB, Nakagawa Y, Manfredi G, Goto Y, Cox GA, Nishino I. 2011. Muscle choline kinase beta defect causes mitochondrial dysfunction and increased mitophagy. Hum Mol Genet 20:3841–3851.

Schagger H, Pfeiffer K. 2000. Supercomplexes in the respiratory chains of yeast and mammalian mitochondria. EMBO J 19:1777–1783.

Trounce IA, Kim YL, Jun AS, Wallace DC. 1996. Assessment of mitochondrial oxidative phosphorylation in patient muscle biopsies, lymphoblasts, and transmitochondrial cell lines. Methods Enzymol 264:484–509.

Tsurusaki Y, Osaka H, Hamanoue H, Shimbo H, Tsuji M, Doi H, Saitsu H, Matsumoto N, Miyake N. 2011. Rapid detection of a mutation causing X-linked leucoencephalopathy by exome sequencing. J Med Genet 48:606–609.

Visapaa I, Fellman V, Vesa J, Dasvarma A, Hutton JL, Kumar V, Payne GS, Makarow M, Van Coster R, Taylor RW, Turnbull DM, Suomalainen A, et al. 2002. GRACILE syndrome, a lethal metabolic disorder with iron overload, is caused by a point mutation in BCS*1L*. Am J Hum Genet 71:863–876.

nature genetics

De novo mutations in the autophagy gene *WDR45* cause static encephalopathy of childhood with neurodegeneration in adulthood

Hirotomo Saitsu[1,10], Taki Nishimura[2,3,10], Kazuhiro Muramatsu[4,10], Hirofumi Kodera[1], Satoko Kumada[5], Kenji Sugai[6], Emi Kasai-Yoshida[5], Noriko Sawaura[4], Hiroya Nishida[7], Ai Hoshino[7], Fukiko Ryujin[8], Seiichiro Yoshioka[8], Kiyomi Nishiyama[1], Yukiko Kondo[1], Yoshinori Tsurusaki[1], Mitsuko Nakashima[1], Noriko Miyake[1], Hirokazu Arakawa[4], Mitsuhiro Kato[9], Noboru Mizushima[2,3] & Naomichi Matsumoto[1]

Static encephalopathy of childhood with neurodegeneration in adulthood (SENDA) is a recently established subtype of neurodegeneration with brain iron accumulation (NBIA)[1–3]. By exome sequencing, we found *de novo* heterozygous mutations in *WDR45* at Xp11.23 in two individuals with SENDA, and three additional *WDR45* mutations were identified in three other subjects by Sanger sequencing. Using lymphoblastoid cell lines (LCLs) derived from the subjects, aberrant splicing was confirmed in two, and protein expression was observed to be severely impaired in all five. *WDR45* encodes WD-repeat domain 45 (WDR45). WDR45 (also known as WIPI4) is one of the four mammalian homologs of yeast Atg18, which has an important role in autophagy[4,5]. Lower autophagic activity and accumulation of aberrant early autophagic structures were demonstrated in the LCLs of the affected subjects. These findings provide direct evidence that an autophagy defect is indeed associated with a neurodegenerative disorder in humans.

NBIA is a heterogeneous group of neurodegenerative diseases that are characterized by a prominent extrapyramidal movement disorder, intellectual deterioration and deposition of iron in the basal ganglia[1–3]. Mutations in several genes involved in diverse cellular processes cause NBIA[6]. SENDA is a recently established subtype of NBIA. SENDA begins with early childhood psychomotor retardation, which remains static until adulthood. Then, during their twenties to early thirties, affected individuals develop sudden-onset progressive dystonia-parkinsonism and dementia. In addition to iron deposition in the globus pallidus and substantia nigra, individuals with SENDA have a distinct pattern on brain magnetic resonance images (MRI) of T1-weighted signal hyperintensity of the substantia nigra, with a central band of hypointensity[1–3,6,7]. SENDA is always sporadic[6,7], suggesting the involvement of *de novo* mutations or autosomal recessive traits. To identify *de novo* or recessive mutations, family-based exome sequencing was performed including the affected individual, an unaffected sibling and the unaffected parents.

A total of 180 and 187 rare protein-altering and splice-site variants were identified per affected subject, which were absent in dbSNP135 data and in 88 in-house control exomes (**Supplementary Table 1**). All genes in each subject were surveyed for *de novo* mutations and compound heterozygous or homozygous mutations that were consistent with an autosomal recessive trait in each family (**Supplementary Table 2**). Two *de novo* and one autosomal recessive candidate mutations were found in subject 1, and a *de novo* candidate mutation was found in subject 2. Only mutations in *WDR45* at Xp11.23, encoding WDR45 (referred to here as WIPI4), were common in the two subjects. A canonical splice-site mutation (c.439+1G>T) was found in subject 1, and a synonymous mutation located at the last base of exon 8 (c.516G>C) was found in subject 2, both of which occurred *de novo* (**Fig. 1a**). Sanger sequencing of *WDR45* in three other affected subjects identified one nonsense and two frameshift mutations (**Fig. 1a**). The c.1033_1034dupAA mutation in subject 5 occurred *de novo*. Parental samples for the other two subjects were unavailable. None of the five mutations were found in 6,500 National Heart, Lung, and Blood Institute (NHLBI) exomes or among our 212 in-house control exomes. All subjects with a *WDR45* mutation are female.

To examine the effects of the mutations on *WDR45* transcription, RT-PCR and sequencing were performed on total RNA extracted from the LCLs of subjects. The c.439+1G>T mutation in subject 1 and the c.516G>C mutation in subject 2 caused 24-bp in-frame and 22-bp

[1]Department of Human Genetics, Graduate School of Medicine, Yokohama City University, Yokohama, Japan. [2]Department of Physiology and Cell Biology, Graduate School and Faculty of Medicine, Tokyo Medical and Dental University, Tokyo, Japan. [3]Department of Biochemistry and Molecular Biology, Graduate School and Faculty of Medicine, The University of Tokyo, Tokyo, Japan. [4]Department of Pediatrics, Gunma University Graduate School of Medicine, Gunma, Japan. [5]Department of Neuropediatrics, Tokyo Metropolitan Neurological Hospital, Tokyo, Japan. [6]Department of Child Neurology, National Center of Neurology and Psychiatry, Tokyo, Japan. [7]Department of Pediatrics, National Rehabilitation Center for Children with Disabilities, Tokyo, Japan. [8]Department of Pediatrics, Shiga University of Medical Science, Shiga, Japan. [9]Department of Pediatrics, Yamagata University Faculty of Medicine, Yamagata, Japan. [10]These authors contributed equally to this work. Correspondence should be addressed to H.S. (hsaitsu@yokohama-cu.ac.jp), N. Mizushima (nmizu@m.u-tokyo.ac.jp) or N. Matsumoto (naomat@yokohama-cu.ac.jp).

Received 24 October 2012; accepted 29 January 2013; published online 24 February 2013; doi:10.1038/ng.2562

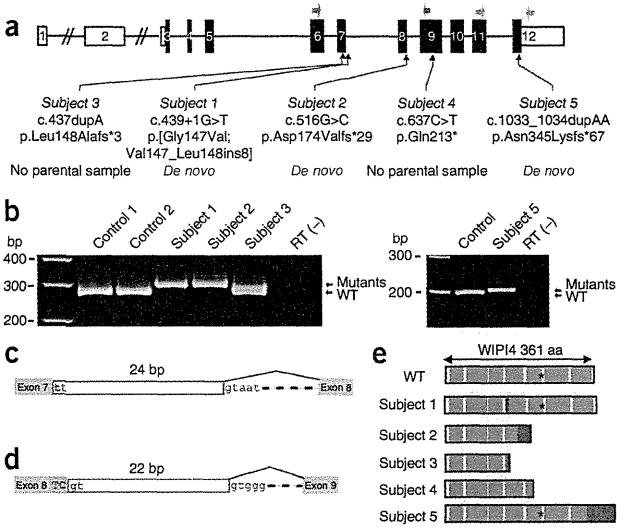

Figure 1 Heterozygous *WDR45* mutations in individuals with SENDA. (**a**) Schematic of *WDR45*, which comprises 12 exons (rectangles). The UTRs and coding region are shown in white and black, respectively. Three mutations were confirmed as *de novo*; the others were unable to be confirmed because parental samples were unavailable. Blue and green arrows indicate the locations of the two sets of primers used in mRNA analysis. (**b**) RT-PCR analysis using the blue primer set (left) and green primer set (right) from **a**. Whereas control cDNA samples showed a single product corresponding to the wild-type allele (WT), an apparently longer product was observed in subjects 1, 2 and 5, indicating that only the transcripts from the mutant allele were expressed. In subject 3, both wild-type and mutant alleles were expressed. Template without reverse transcriptase was used as a negative control, RT(–). (**c**) Schematic of the mutant transcript resulting from the c.439+1G>T mutation (red) in subject 1. A 24-bp insertion caused by the use of a cryptic splice donor site within intron 7 was observed, resulting in a p.Gly147Val substitution followed by an in-frame eight-amino-acid insertion (p.[Gly147Val; Val147_Leu148ins8]). (**d**) Schematic of the mutant transcript resulting from the c.516G>C mutation (red) in subject 2. A 22-bp insertion from the use of a cryptic splice donor site within intron 8 was observed, leading to a frameshift (p.Asp174Valfs*29). (**e**) Schematic of mutant WIPI4 proteins. β-propeller structures and additional residues caused by mutations are colored in blue and red, respectively. The amino-acid residues of the mutant protein predicted from cDNA sequences are shown in relation to seven–β propeller structures[13–15]. An asterisk indicates the position of the FRRG motifs.

frameshift insertions, respectively (**Fig. 1b–d** and **Supplementary Fig. 1**). The c.437dupA, c.637C>T and c.1033_1034dupAA mutations were confirmed in the transcripts (**Fig. 1b** and **Supplementary Fig. 1**). Theoretically, mutant WIPI4 would be severely truncated in subjects 2, 3 and 4 and relatively conserved in subjects 1 and 5 (**Fig. 1e**). As human female cells are subject to X-chromosome inactivation, subjects with a *WDR45* mutation may have two cell populations: one expressing a wild-type allele and the other expressing a mutant allele. Notably, whereas both wild-type and mutant alleles were expressed in the LCLs of subject 3, the LCLs of the other four affected subjects exclusively expressed mutant transcripts, suggesting that the wild-type alleles underwent X inactivation in most cells (**Fig. 1b** and **Supplementary Fig. 1**). In fact, X-inactivation analysis with genomic DNA from peripheral leukocytes showed a skewed pattern in subjects 2, 4 and 5 (analysis was non-informative in subject 1) (**Supplementary Table 3**). However, it is unknown whether the wild-type allele underwent X inactivation in brain tissues as in LCLs and leukocytes from the subjects.

The clinical features of the individuals with SENDA possessing *WDR45* mutations are summarized in **Table 1** (see also the **Supplementary Note**). Subjects 1 and 3 have been described recently[7,8]. These individuals showed psychomotor developmental delay from infancy and severe intellectual disability, while their motor function gradually developed. In adulthood, severe progressive dystonia-parkinsonism and dementia developed. Four of the subjects became bedridden within a few years of onset of cognitive decline. In all subjects, blood concentrations of ceruloplasmin, copper, iron, ferritin and lactate acid were normal. Brain MRI showed T1-weighted signal hyperintensity in the substantia nigra with a central T1-weighted hypointensity band (**Fig. 2a–e**) and T2-weighted signal hypointensity, suggesting iron deposition in the globus pallidus and substantia nigra (**Fig. 2f–h**), which are characteristic of SENDA. In addition, significant cerebral atrophy was found (**Fig. 2i,j**). Substantial differences in the severity of clinical findings were not observed among the five subjects.

WIPI1, WIPI2, WIPI3 and WIPI4, mammalian Atg18 homologs, have an important role in the autophagy pathway[4,5]. Autophagy is the major intracellular degradation system by which cytoplasmic materials are enclosed by double-membrane structures called autophagosomes and subsequently delivered to lysosomes for degradation[9]. More than 30 autophagy-related (ATG) genes have been identified in yeast[10,11], many of which are conserved in higher eukaryotes and are essential for the formation of the autophagosome[10,12]. These factors include subunits of the class III phosphatidylinositol 3-kinase complex, and generation of the lipid phosphatidylinositol 3-phosphate is essential for autophagosome formation. Atg18 in yeast and WIPI subunits in mammals associate with membranes through a phosphoinositide-binding motif (FRRG) within a seven–β propeller structure[13–15]. Atg18 and WIPI proteins also interact with Atg2 and its homologs in yeast and mammalian cells, respectively[16,17]. Autophagic activity in relation to WIPI4 expression was examined using LCLs from the subjects. Immunoblot analysis of WIPI4 showed lower expression in all five subjects compared to unaffected individuals (**Fig. 3a**). Although mutant WIPI4 protein sequence was relatively conserved in subjects 1 and 5, the expression of mutant WIPI4 in both subjects was severely decreased, similar to that of subjects 2, 3 and 4, in whom mutant WIPI4 was truncated. This suggests that all the mutant proteins are structurally unstable and undergo degradation. To examine the effect of the *WDR45* mutations on autophagy, an autophagic flux assay was performed using LCLs. When lysosomal degradation was blocked by the lysosomal inhibitor chloroquine, the amount of LC3-II (the membrane-bound form) was higher than in cells without the inhibitor, as for control LCLs (**Fig. 3b** and **Supplementary Fig. 2**)[18]. The differences in LC3-II amounts between samples with and without chloroquine represent the amount of LC3 on autophagic structures delivered to lysosomes for degradation[18]. In the LCLs from affected subjects, accumulation of LC3-II was observed, even under normal conditions, which was more apparent when autophagy was induced by the mTORC1 inhibitor Torin1 (**Supplementary Fig. 2a–d**). The increase in the LC3-II amount by concomitant chloroquine treatment was significant or tended to be suppressed in the LCLs from affected subjects, suggesting that the autophagic flux was blocked, probably incompletely, at an intermediate step of autophagosome formation (**Fig. 3b** and **Supplementary Fig. 2e**).

Consistent with the immunoblot analysis, immunofluorescence microscopy showed the accumulation of LC3-containing autophagic

Table 1 Clinical features of subjects with SENDA with a *WDR45* mutation

	Subject 1	Subject 2	Subject 3	Subject 4	Subject 5
Age	33 years	28 years	40 years	51 years	33 years
Sex	Female	Female	Female	Female	Female
Mutation	c.439+1G>T	c.516G>C	c.437dupA	c.637C>T	c.1033_1034dupAA
Protein alteration	p.[Gly147Val; Val147_Leu148ins8]	p.Asp174Valfs*29	p.Leu148Alafs*3	p.Gln213*	p.Asn345Lysfs*67
Neurological symptoms					
Current status	Bedridden	Wheelchair	Bedridden	Bedridden	Bedridden
Initial symptom	Psychomotor retardation	Psychomotor retardation	Psychomotor retardation	Psychomotor retardation	Psychomotor retardation
Initial walking	3 years	2 years 7 months	2 years 2 months	1 year 6 months	1 year 6 months
Speech ability	No word	One word	No word	Two-word sentences	Few words
Cognitive dysfunction during childhood	Nonprogressive	Nonprogressive	Nonprogressive	Nonprogressive	Nonprogressive
Start of cognitive decline	26 years	25 years	30 years	24 years	23 years
Period until bedridden after decline	4 years	–	3 years	1 year	6 years
Dystonia	+	+	+	+	+
Parkinsonism	Rigidity, akinesia	Rigidity, akinesia	Rigidity	Rigidity	Rigidity, tremor, impairment of postural reflex
Progressive dementia during adulthood	+	+	+	+	+
Psychiatric symptoms	Aggressive behaviors	Aggressive behaviors	None	None	Anxiety
Epileptic seizure	+	+	FS	None	+
Radiological features					
MRI					
Iron deposition	Globus pallidus, substantia nigra	Globus pallidus, substantia nigra	Globus pallidus, substantia nigra	Globus pallidus, substantia nigra	Globus pallidus, substantia nigra
Central band of T1 hypointensity	+	+	+	+	+
Cerebral atrophy	Moderate at 25 years, remarkable at 32 and 33 years	Moderate at 25 and 27 years	Mild at 33 years, remarkable at 39 years	Mild at 27 years, remarkable at 46 years	Remarkable at 33 years
Eye of the tiger sign	–	–	–	–	–
White matter involvement	–	–	–	–	–
Cerebellar atrophy	Mild at 25, 32 and 33 years	Mild at 25 and 27 years	Mild at 33 and 39 years	Mild at 27 and 46 years	Mild at 33 years
CT findings	High density in globus pallidus	Mild high density in substantia nigra	High density in substantia nigra	High density in ventral midbrain	High density in globus pallidus
Neurophysiological examination					
EEG	Bilateral frontal spike	Bilateral frontal spike, low voltage, slow wave	Low voltage	Abnormal	Abnormal
EMG	NE	NE	Dystonic pattern	Normal	NE
VEP	Normal	NE	Prolonged P100 latency	NE	Normal
ABR	Low amplitude, normal latency	NE	No response at 100 dB	NE	NE

FS, febrile seizure; EEG, electroencephalogram; EMG, electromyogram; VEP, visual evoked potential; ABR, auditory brainstem response; NE, not examined.

structures in the LCLs from affected subjects, some of which were abnormally enlarged compared with those observed in control LCLs (**Fig. 3c,d**). Therefore, we examined whether these LC3-positive structures in fact included premature or abnormal autophagic structures. A recent study showed that knockdown of *Wdr45* in rat kidney cells and mutation in *epg-6* (encoding a WIPI4 homolog)

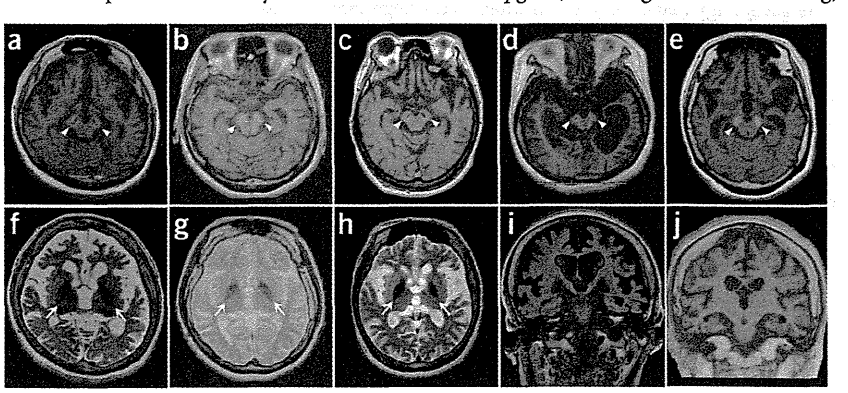

Figure 2 Brain MRIs at 3.0 T and 1.5 T. (**a–e**) T1-weighted imaging shows hyperintensity of the substantia nigra with a central band of T1-weighted hypointensity (arrowheads). Images are shown for subject 1 at 33 years (**a**), subject 2 at 25 years (**b**), subject 3 at 39 years (**c**), subject 4 at 46 years (**d**) and subject 5 at 33 years (**e**). (**f–h**) T2-weighted imaging shows marked hypointensity of the globus pallidus (arrows), suggesting iron deposition. Cerebral atrophy and mild cerebellar atrophy are also seen. Images are shown for subject 1 (**f**), subject 2 (**g**) and subject 3 (**h**). (**i,j**) The fluid attenuated inversion recovery (FLAIR) image of subject 1 (**i**) and the T1-weighted FLAIR coronal image of subject 2 (**j**) also show cerebral atrophy.

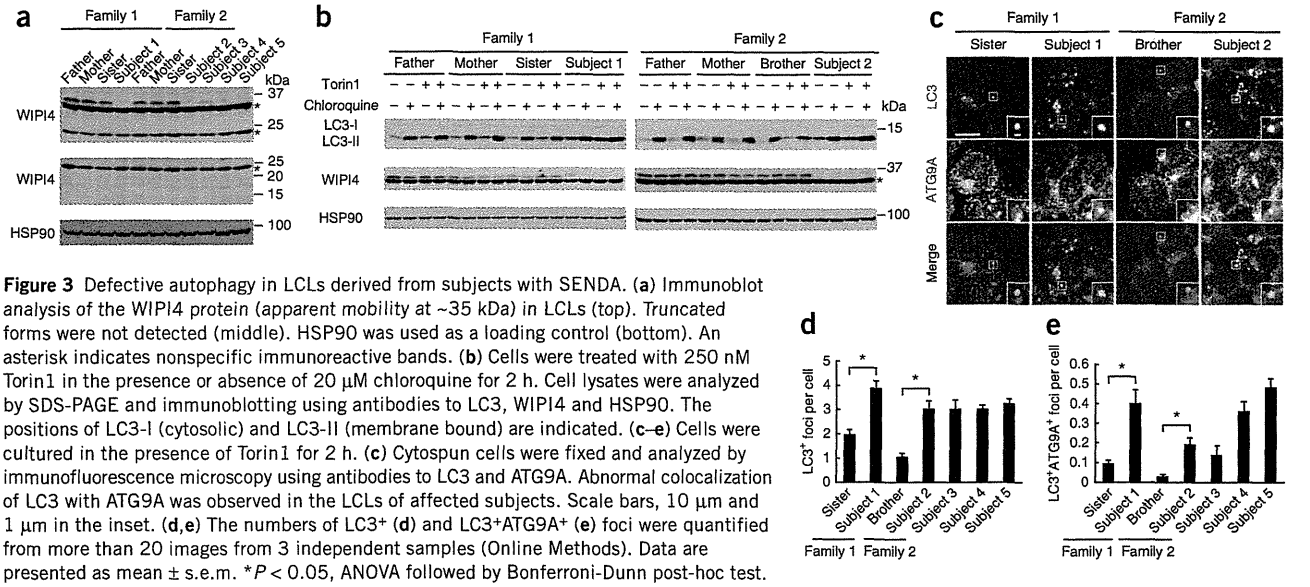

Figure 3 Defective autophagy in LCLs derived from subjects with SENDA. (**a**) Immunoblot analysis of the WIPI4 protein (apparent mobility at ~35 kDa) in LCLs (top). Truncated forms were not detected (middle). HSP90 was used as a loading control (bottom). An asterisk indicates nonspecific immunoreactive bands. (**b**) Cells were treated with 250 nM Torin1 in the presence or absence of 20 μM chloroquine for 2 h. Cell lysates were analyzed by SDS-PAGE and immunoblotting using antibodies to LC3, WIPI4 and HSP90. The positions of LC3-I (cytosolic) and LC3-II (membrane bound) are indicated. (**c–e**) Cells were cultured in the presence of Torin1 for 2 h. (**c**) Cytospun cells were fixed and analyzed by immunofluorescence microscopy using antibodies to LC3 and ATG9A. Abnormal colocalization of LC3 with ATG9A was observed in the LCLs of affected subjects. Scale bars, 10 μm and 1 μm in the inset. (**d**,**e**) The numbers of $LC3^+$ (**d**) and $LC3^+ATG9A^+$ (**e**) foci were quantified from more than 20 images from 3 independent samples (Online Methods). Data are presented as mean ± s.e.m. $^*P < 0.05$, ANOVA followed by Bonferroni-Dunn post-hoc test.

in *Caenorhabditis elegans* cause accumulation of early autophagic structures[5]. One supposed function of WIPI4 (Epg-6) is to regulate the distribution of ATG9A-marked vesicles[5], which transiently localize to the autophagosome formation site and induce autophagosome formation[19,20]. ATG9A is absent from completed autophagosomes in mammalian cells; therefore, colocalization of ATG9A and LC3 is rare. However, enlarged structures positive for both ATG9A and LC3 accumulated in LCLs from all five subjects (**Fig. 3c,e**), indicating improper autophagosome formation.

The importance of the housekeeping activity of autophagy in neurons, as well as the ubiquitin-proteasome system, has been demonstrated in mice. Mice lacking autophagy in the central nervous system developed progressive motor and behavioral deficits[21,22]. Histologically, inclusion bodies containing polyubiquitinated proteins were observed in neurons, and their size and number increased with age[21,22]. Neuronal cell death was observed in subsets of neurons[21,22], implying that the impairment of autophagy contributes to the pathogenesis of neurodegenerative disorders. Indeed, dysregulation of autophagy has been suggested in various neurodegenerative disorders in humans[23]. In addition, mutations in *PARK2* and *PINK1*, both of which cause familial Parkinson's disease[24,25], impair the selective autophagic degradation of damaged mitochondria, called mitophagy (PARK2, also called Parkin, is recruited to damaged mitochondria in a PINK1-dependent manner)[26,27]. However, a direct link between the core autophagy machinery and human neurodegenerative disorders has not been reported. Here, we showed that mutations in *WDR45*, a core autophagy gene, result in a neurodegenerative disorder. Notably, the autophagy defects were partial, implying that some autophagic activity could be maintained in the neurons of affected subjects. We hypothesize that this might be a possible explanation of why childhood intellectual disability in individuals with SENDA remains static until adulthood, unlike in other forms of NBIA[1–3]. In contrast to heterozygous *WDR45* mutations in females, hemizygous germline mutations in males, leading to the expression of mutant *WDR45* in all cells, possibly cause lethal phenotypes from complete loss of *WDR45* function, as mice defective in autophagy die shortly after birth[28–32]. While this paper was under review, Haack *et al.* reported *WDR45* mutations in 20 subjects, including 3 males, 1 of whom possessed a mutation that was somatic mosaic, supporting the idea that male germline mutations could be lethal[33].

WDR45 is widely expressed in human tissues, with the highest expression found in skeletal muscle[34]. Nevertheless, SENDA phenotypes seem to be limited to the brain. These facts may reflect cell type–dependent differences: autophagy could be more important in neurons (non-dividing, terminally differentiated cells) than in LCLs (rapidly dividing cells). In addition, it is possible that the other WIPI homologs (WIPI1, WIPI2 and WIPI3) could compensate for the deficiency in WIPI4 in a cell type–dependent manner, and the relative contribution of WIPI4 among WIPI factors may be high in neurons.

In conclusion, heterozygous mutations of X-linked *WDR45*, a core autophagy gene, were identified in SENDA, providing direct evidence that an autophagy defect is indeed associated with a neurodegenerative disorder in humans.

URLs. NHLBI Exome Sequencing Project, http://evs.gs.washington.edu/EVS/; Picard, http://picard.sourceforge.net/; SAMtools, http://samtools.sourceforge.net/; dbSNP, http://www.ncbi.nlm.nih.gov/projects/SNP/.

METHODS

Methods and any associated references are available in the online version of the paper.

Accession codes. Reference sequences are available from GenBank for *Homo sapiens WDR45* transcript variant 1 mRNA (NM_007075.3) and WIPI4 isoform 1 (NP_009006.2).

Note: Supplementary information is available in the online version of the paper.

ACKNOWLEDGMENTS

We would like to thank the individuals with SENDA and their families for their participation in this study. We thank M. Shiina and K. Ogata for their helpful comments on the protein structure. This work was supported by research grants from the Ministry of Health, Labour and Welfare (H.S., N. Miyake and N. Matsumoto), the Japan Science and Technology Agency (N. Matsumoto) and the Strategic Research Program for Brain Sciences (N. Matsumoto) and by a Grant-in-Aid for Scientific Research on Innovative Areas (Transcription Cycle) from the Ministry of Education, Culture, Sports, Science and Technology of Japan

(N. Matsumoto), a Grant-in-Aid for Scientific Research from the Japan Society for the Promotion of Science (N. Matsumoto), a Grant-in-Aid for Young Scientists from the Japan Society for the Promotion of Science (H.S. and N. Miyake), the Funding Program for Next-Generation World-Leading Researchers (N. Mizushima) and a grant from the Takeda Science Foundation (N. Miyake, N. Mizushima and N. Matsumoto).

AUTHOR CONTRIBUTIONS

H.S., N. Mizushima and N. Matsumoto designed and directed the study. H.S., T.N., K.M., N. Mizushima and N. Matsumoto wrote the manuscript. K.M., S.K., K.S., E.K.-Y., N.S., H.N., A.H., F.R., S.Y., H.A. and M.K. collected samples and provided the subjects' clinical information. H.S., H.K., K.N., Y.T., M.N. and N. Miyake performed exome sequencing and Sanger sequencing. H.S. and K.N. performed the RNA analysis. Y.K. performed the X-inactivation analysis. T.N. and N. Mizushima analyzed protein expression and autophagic activity.

COMPETING FINANCIAL INTERESTS

The authors declare no competing financial interests.

1. Gregory, A., Polster, B.J. & Hayflick, S.J. Clinical and genetic delineation of neurodegeneration with brain iron accumulation. *J. Med. Genet.* **46**, 73–80 (2009).
2. Kruer, M.C. *et al.* Neuroimaging features of neurodegeneration with brain iron accumulation. *AJNR Am. J. Neuroradiol.* **33**, 407–414 (2012).
3. Schneider, S.A. & Bhatia, K.P. Syndromes of neurodegeneration with brain iron accumulation. *Semin. Pediatr. Neurol.* **19**, 57–66 (2012).
4. Polson, H.E. *et al.* Mammalian Atg18 (WIPI2) localizes to omegasome-anchored phagophores and positively regulates LC3 lipidation. *Autophagy* **6**, 506–522 (2010).
5. Lu, Q. *et al.* The WD40 repeat PtdIns(3)P-binding protein EPG-6 regulates progression of omegasomes to autophagosomes. *Dev. Cell* **21**, 343–357 (2011).
6. Gregory, A. & Hayflick, S.J. Genetics of neurodegeneration with brain iron accumulation. *Curr. Neurol. Neurosci. Rep.* **11**, 254–261 (2011).
7. Kimura, Y. *et al.* MRI, MR spectroscopy, and diffusion tensor imaging findings in patient with static encephalopathy of childhood with neurodegeneration in adulthood (SENDA). *Brain Dev.* published online; doi:10.1016/j.braindev.2012.07.008 (11 August 2012).
8. Kasai-Yoshida, E. *et al.* First video report of static encephalopathy of childhood with neurodegeneration in adulthood. *Mov. Disord.* published online; doi:10.1002/mds.25158 (6 February 2013).
9. Mizushima, N. & Komatsu, M. Autophagy: renovation of cells and tissues. *Cell* **147**, 728–741 (2011).
10. Nakatogawa, H., Suzuki, K., Kamada, Y. & Ohsumi, Y. Dynamics and diversity in autophagy mechanisms: lessons from yeast. *Nat. Rev. Mol. Cell Biol.* **10**, 458–467 (2009).
11. Xie, Z. & Klionsky, D.J. Autophagosome formation: core machinery and adaptations. *Nat. Cell Biol.* **9**, 1102–1109 (2007).
12. Mizushima, N., Yoshimori, T. & Ohsumi, Y. The role of Atg proteins in autophagosome formation. *Annu. Rev. Cell Dev. Biol.* **27**, 107–132 (2011).
13. Baskaran, S., Ragusa, M.J., Boura, E. & Hurley, J.H. Two-site recognition of phosphatidylinositol 3-phosphate by PROPPINs in autophagy. *Mol. Cell* **47**, 339–348 (2012).
14. Krick, R. *et al.* Structural and functional characterization of the two phosphoinositide binding sites of PROPPINs, a β-propeller protein family. *Proc. Natl. Acad. Sci. USA* **109**, E2042–E2049 (2012).
15. Watanabe, Y. *et al.* Structure-based analyses reveal distinct binding sites for Atg2 and phosphoinositides in Atg18. *J. Biol. Chem.* **287**, 31681–31690 (2012).
16. Suzuki, K., Kubota, Y., Sekito, T. & Ohsumi, Y. Hierarchy of Atg proteins in pre-autophagosomal structure organization. *Genes Cells* **12**, 209–218 (2007).
17. Velikkakath, A.K., Nishimura, T., Oita, E., Ishihara, N. & Mizushima, N. Mammalian Atg2 proteins are essential for autophagosome formation and important for regulation of size and distribution of lipid droplets. *Mol. Biol. Cell* **23**, 896–909 (2012).
18. Mizushima, N., Yoshimori, T. & Levine, B. Methods in mammalian autophagy research. *Cell* **140**, 313–326 (2010).
19. Itakura, E., Kishi-Itakura, C., Koyama-Honda, I. & Mizushima, N. Structures containing Atg9A and the ULK1 complex independently target depolarized mitochondria at initial stages of Parkin-mediated mitophagy. *J. Cell Sci.* **125**, 1488–1499 (2012).
20. Orsi, A. *et al.* Dynamic and transient interactions of Atg9 with autophagosomes, but not membrane integration, are required for autophagy. *Mol. Biol. Cell* **23**, 1860–1873 (2012).
21. Hara, T. *et al.* Suppression of basal autophagy in neural cells causes neurodegenerative disease in mice. *Nature* **441**, 885–889 (2006).
22. Komatsu, M. *et al.* Loss of autophagy in the central nervous system causes neurodegeneration in mice. *Nature* **441**, 880–884 (2006).
23. Menzies, F.M., Moreau, K. & Rubinsztein, D.C. Protein misfolding disorders and macroautophagy. *Curr. Opin. Cell Biol.* **23**, 190–197 (2011).
24. Valente, E.M. *et al.* Hereditary early-onset Parkinson's disease caused by mutations in *PINK1*. *Science* **304**, 1158–1160 (2004).
25. Kitada, T. *et al.* Mutations in the *parkin* gene cause autosomal recessive juvenile parkinsonism. *Nature* **392**, 605–608 (1998).
26. Youle, R.J. & van der Bliek, A.M. Mitochondrial fission, fusion, and stress. *Science* **337**, 1062–1065 (2012).
27. Youle, R.J. & Narendra, D.P. Mechanisms of mitophagy. *Nat. Rev. Mol. Cell Biol.* **12**, 9–14 (2011).
28. Kuma, A. *et al.* The role of autophagy during the early neonatal starvation period. *Nature* **432**, 1032–1036 (2004).
29. Saitoh, T. *et al.* Loss of the autophagy protein Atg16L1 enhances endotoxin-induced IL-1β production. *Nature* **456**, 264–268 (2008).
30. Saitoh, T. *et al.* Atg9a controls dsDNA-driven dynamic translocation of STING and the innate immune response. *Proc. Natl. Acad. Sci. USA* **106**, 20842–20846 (2009).
31. Sou, Y.S. *et al.* The Atg8 conjugation system is indispensable for proper development of autophagic isolation membranes in mice. *Mol. Biol. Cell* **19**, 4762–4775 (2008).
32. Komatsu, M. *et al.* Impairment of starvation-induced and constitutive autophagy in *Atg7*-deficient mice. *J. Cell Biol.* **169**, 425–434 (2005).
33. Haack, T.B. *et al.* Exome sequencing reveals *de novo WDR45* mutations causing a phenotypically distinct, X-linked dominant form of NBIA. *Am. J. Hum. Genet.* **91**, 1144–1149 (2012).
34. Proikas-Cezanne, T. *et al.* WIPI-1α (WIPI49), a member of the novel 7-bladed WIPI protein family, is aberrantly expressed in human cancer and is linked to starvation-induced autophagy. *Oncogene* **23**, 9314–9325 (2004).

ONLINE METHODS

Subjects. We analyzed five Japanese individuals with SENDA. Diagnosis was made on the basis of clinical features, including psychomotor retardation at early childhood that was static for decades and severe progressive dystonia-parkinsonism and dementia after several decades, as well as characteristic findings on brain MRI scans. Genomic DNA was isolated from blood leukocytes according to standard protocols. The Institutional Review Board of Yokohama City University approved the experimental protocols. Informed consent was obtained for all individuals included in this study in agreement with the requirements of Japanese regulations. Clinical information on the subjects with a *WDR45* mutation is presented in **Table 1** and in the **Supplementary Note**.

Mutation screening. Mutation screening of exons 3–12 covering the *WDR45* coding region (of transcript variant 1, GenBank accession NM_007075.3) was performed by direct sequencing. PCR was performed in a 20-μl mixture containing 1 μl of genomic DNA, 1× PCR Buffer for KOD FX NEO, 0.4 mM of each dNTP, 0.3 μM of each primer and 0.4 U of KOD FX NEO polymerase (Toyobo). Details on PCR conditions and primer sequences are given in **Supplementary Table 4**.

Exome sequencing. Genomic DNA was captured using the SureSelect Human All Exon v4 kit (51 Mb; Agilent Technologies) and sequenced with four samples per lane on an Illumina HiSeq2000 with 101-bp paired-end reads. Image analysis and base calling were performed by sequence control software real-time analysis and CASAVA software v1.8 (Illumina). Reads were aligned to GRCh37 with Novoalign (Novocraft Technologies). Duplicate reads were marked using Picard (see URLs) and excluded from downstream analysis. After merging the BAM files of all members in each family using SAMtools, local realignments around indels and base quality score recalibration were performed with the Genome Analysis Toolkit (GATK)[35]. Single-nucleotide variants and small indels were identified using the GATK UnifiedGenotyper and filtered according to the Broad Institute's best-practice guidelines (version 3). Variants registered in dbSNP135, which were not flagged as clinically associated, were excluded. Variants that passed the filters were annotated using ANNOVAR[36].

RNA analysis. LCLs were established from five affected subjects and their family members. RT-PCR using total RNA extracted from LCLs was performed as previously described[37]. Briefly, 4 μg of total RNA extracted with an RNeasy Plus Mini kit (Qiagen) was subjected to reverse transcription, and 2 μl of cDNA was used for PCR. Details on primer sequences and PCR conditions are given in **Supplementary Table 4**. PCR products were electrophoresed in a 10% polyacrylamide gel and sequenced.

X-inactivation analysis. The X-inactivation pattern was studied using the human androgen receptor (HUMARA) assay and a fragile X mental retardation (*FRAXA*) locus methylation assay as previously described[38–40]. Briefly, genomic DNA from the subjects, a control male and a control female was digested with two methylation-sensitive enzymes, HpaII and HhaI. Details on PCR conditions and primer sequences are given in **Supplementary Table 4**. Fluorescently labeled products were analyzed on an ABI PRISM 3500 Genetic Analyzer with GeneMapper Software version 4.0 (Applied Biosystems). X-inactivation ratios of less than or equal to 80:20 were considered to represent a random pattern, ratios greater than 80:20 were considered to represent a skewed pattern, and ratios greater than 90:10 were considered to represent a markedly skewed pattern[38].

Cell culture. LCLs were cultured in RPMI 1640 supplemented with 10% FBS, L-glutamine, tylosin and antibiotic-antimycotic solution in a 5% CO_2 incubator.

Immunoblotting. An affinity-purified rabbit polyclonal antibody against WIPI4 peptide antigen (CFPDNPRKLFEFDTRDNP, amino acids 129–145) was generated by Medical & Biological Laboratories. The specificity of the antibody was tested using lysate from HeLa cells in which *WDR45* was knocked down. For immunoblot analysis, cells were lysed with lysis buffer (50 mM Tris-HCl, pH 7.5, 150 mM NaCl, 1 mM EDTA, 1% Triton X-100, 1 mM phenylmethanesulfonyl fluoride and a protease inhibitor cocktail (Complete EDTA-free protease inhibitor, Roche)). Cell lysates were clarified by centrifugation at 12,000*g* for 20 min and analyzed by SDS-PAGE and immunoblotting using antibodies to WIPI4, LC3 (ref. 41) and HSP90 (BD Transduction Laboratories, 610418). Signal intensities were analyzed using a LAS-3000 mini imaging analyzer and Multi Gauge software version 3.0 (Fujifilm). Contrast and brightness adjustments were applied to the images using Photoshop 7.0.1 (Adobe Systems).

Fluorescence microscopy. LCLs were spun onto a glass slide at 500 RPM (28*g*) for 1 min in a Shandon Cytospin 4 cytofuge (Thermo Electron). Cells were fixed with 4% paraformaldehyde, permeabilized using 50 μg/ml digitonin and then stained with antibodies to LC3 (clone 1703, Cosmo Bio) and Atg9A[19]. Cells were observed with a confocal laser microscope (FV1000D IX81, Olympus) using a 60× PlanApoN oil immersion lens (1.42 numerical aperture (N.A.), Olympus). For final output, images were processed using Adobe Photoshop 7.0.1 software. The number of staining foci was determined as follows: foci were extracted using the top hat operation (parameter of 300 × 300 pixel area), and a binary image was created. Small foci (with an area of less than 10 × 10 pixels) were removed using an open operation. The number of foci was counted using the integrated morphometry analysis program. False foci were removed by comparison with the original image.

Statistical analysis. Differences were analyzed statistically using unpaired *t* tests or analysis of variance (ANOVA) with a Bonferroni-Dunn post-hoc test.

35. DePristo, M.A. *et al.* A framework for variation discovery and genotyping using next-generation DNA sequencing data. *Nat. Genet.* **43**, 491–498 (2011).
36. Wang, K., Li, M. & Hakonarson, H. ANNOVAR: functional annotation of genetic variants from high-throughput sequencing data. *Nucleic Acids Res.* **38**, e164 (2010).
37. Saitsu, H. *et al. STXBP1* mutations in early infantile epileptic encephalopathy with suppression-burst pattern. *Epilepsia* **51**, 2397–2405 (2010).
38. Kondo, Y. *et al.* A family of oculofaciocardiodental syndrome (OFCD) with a novel *BCOR* mutation and genomic rearrangements involving *NHS*. *J. Hum. Genet.* **57**, 197–201 (2012).
39. Allen, R.C., Zoghbi, H.Y., Moseley, A.B., Rosenblatt, H.M. & Belmont, J.W. Methylation of HpaII and HhaI sites near the polymorphic CAG repeat in the human androgen-receptor gene correlates with X chromosome inactivation. *Am. J. Hum. Genet.* **51**, 1229–1239 (1992).
40. Carrel, L. & Willard, H.F. An assay for X inactivation based on differential methylation at the fragile X locus, *FMR1*. *Am. J. Med. Genet.* **64**, 27–30 (1996).
41. Hosokawa, N., Hara, Y. & Mizushima, N. Generation of cell lines with tetracycline-regulated autophagy and a role for autophagy in controlling cell size. *FEBS Lett.* **580**, 2623–2629 (2006).

Mutations in *B3GALT6*, which Encodes a Glycosaminoglycan Linker Region Enzyme, Cause a Spectrum of Skeletal and Connective Tissue Disorders

Masahiro Nakajima,[1,21] Shuji Mizumoto,[2,21] Noriko Miyake,[3,21] Ryo Kogawa,[2] Aritoshi Iida,[1] Hironori Ito,[4] Hiroshi Kitoh,[5] Aya Hirayama,[6] Hiroshi Mitsubuchi,[7] Osamu Miyazaki,[8] Rika Kosaki,[9] Reiko Horikawa,[10] Angeline Lai,[11] Roberto Mendoza-Londono,[12] Lucie Dupuis,[12] David Chitayat,[12] Andrew Howard,[13] Gabriela F. Leal,[14] Denise Cavalcanti,[15] Yoshinori Tsurusaki,[3] Hirotomo Saitsu,[3] Shigehiko Watanabe,[16] Ekkehart Lausch,[17] Sheila Unger,[18] Luisa Bonafé,[19] Hirofumi Ohashi,[16] Andrea Superti-Furga,[19] Naomichi Matsumoto,[3] Kazuyuki Sugahara,[2] Gen Nishimura,[20] and Shiro Ikegawa[1,*]

Proteoglycans (PGs) are a major component of the extracellular matrix in many tissues and function as structural and regulatory molecules. PGs are composed of core proteins and glycosaminoglycan (GAG) side chains. The biosynthesis of GAGs starts with the linker region that consists of four sugar residues and is followed by repeating disaccharide units. By exome sequencing, we found that *B3GALT6* encoding an enzyme involved in the biosynthesis of the GAG linker region is responsible for a severe skeletal dysplasia, spondyloepimetaphyseal dysplasia with joint laxity type 1 (SEMD-JL1). *B3GALT6* loss-of-function mutations were found in individuals with SEMD-JL1 from seven families. In a subsequent candidate gene study based on the phenotypic similarity, we found that *B3GALT6* is also responsible for a connective tissue disease, Ehlers-Danlos syndrome (progeroid form). Recessive loss-of-function mutations in *B3GALT6* result in a spectrum of disorders affecting a broad range of skeletal and connective tissues characterized by lax skin, muscle hypotonia, joint dislocation, and spinal deformity. The pleiotropic phenotypes of the disorders indicate that *B3GALT6* plays a critical role in a wide range of biological processes in various tissues, including skin, bone, cartilage, tendon, and ligament.

Skeletal dysplasias represent a vast collection of genetic disorders of the skeleton, currently divided into 40 groups.[1] Spondyloepimetaphyseal dysplasia (SEMD) is one group (group 13) of skeletal dysplasia that contains more than a dozen distinctive diseases. SEMD with joint laxity (SEMD-JL) is a subgroup of SEMD that consists of type 1 (SEMD-JL1 [MIM 271640]) and type 2 (SEMD-JL2 [MIM 603546]). SEMD-JL1 or SEMD-JL Beighton type is an autosomal-recessive disorder that shows mild craniofacial dysmorphism (prominent eye, blue sclera, long upper lip, small mandible with cleft palate) and spatulate finger with short nail.[2] The large joints of individuals with SEMD-JL1 are variably affected with hip dislocation, elbow contracture secondary to radial head dislocation, and clubfeet. Joint laxity is particularly prominent in the hands. Skeletal changes of SEMD-JL1 are characterized by moderate platyspondyly with anterior projection of the vertebral bodies, hypoplastic ilia, and mild metaphyseal flaring.[3] Kyphoscoliosis progresses with age, leading to a short trunk, whereas platyspondyly become less conspicuous and the vertebral bodies appear squared in shape with age. Recently, dominant kinesin family member 22 (*KIF22* [MIM 603213]) mutations have been found in SEMD-JL2;[4,5] however, the genetic basis of SEMD-JL1 remains unknown.

To identify the SEMD-JL1-causing mutation, we performed whole-exome sequencing experiments. We recruited seven individuals with SEMD-JL1 from five unrelated Japanese families (F1–F5) and a Singapore/Japanese family (F6) (Table 1). One family (F1) had a pair of affected sibs (P1 and P2) from nonconsanguineous parents. Genomic DNA was extracted by standard procedures

[1]Laboratory for Bone and Joint Diseases, Center for Integrative Medical Sciences, RIKEN, Tokyo 108-8639, Japan; [2]Laboratory of Proteoglycan Signaling and Therapeutics, Frontier Research Center for Post-Genomic Science and Technology, Graduate School of Life Science, Hokkaido University, Sapporo 001-0021, Japan; [3]Department of Human Genetics, Yokohama City University Graduate School of Medicine, Yokohama 236-0004, Japan; [4]Department of Orthopaedic Surgery, Central Hospital, Aichi Prefectural Colony, Kasugai 480-0392, Japan; [5]Department of Orthopaedic Surgery, Nagoya University School of Medicine, Nagoya 466-8550, Japan; [6]Department of Pediatrics, Akita Prefectural Center on Development and Disability, Akita 010-1407, Japan; [7]Department of Neonatology, Kumamoto University Hospital, Kumamoto 860-8556, Japan; [8]Department of Radiology, National Center for Child Health and Development, Tokyo 157-8535, Japan; [9]Division of Medical Genetics, National Center for Child Health and Development, Tokyo 157-8535, Japan; [10]Division of Endocrinology and Metabolism, National Center for Child Health and Development, Tokyo 157-8535, Japan; [11]Department of Paediatric Medicine, KK Women's and Children's Hospital, Singapore 229899, Singapore; [12]Department of Paediatrics, The Hospital for Sick Children and University of Toronto, Toronto, ON M5G 1X8, Canada; [13]Department of Surgery, The Hospital for Sick Children and University of Toronto, Toronto, ON M5G 1X8, Canada; [14]The Professor Fernando Figueira Integral Medicine Institute (IMIP), Recife, PE 50070-550, Brazil; [15]Skeletal Dysplasia Group, Department of Medical Genetics, Faculty of Medical Sciences, State University of Campinas (UNICAMP), Campinas, SP 13083-970, Brazil; [16]Division of Medical Genetics, Saitama Children's Medical Center, Saitama 339-8551, Japan; [17]Division of Paediatric Genetics, Centre for Pediatrics and Adolescent Medicine, University of Freiburg, Freiburg 79106, Germany; [18]Medical Genetics Service, University of Lausanne, CHUV, Lausanne 1011, Switzerland; [19]Department of Pediatrics, University of Lausanne, CHUV, Lausanne 1011, Switzerland; [20]Department of Pediatric Imaging, Tokyo Metropolitan Children's Medical Center, Fuchu 183-8561, Japan
[21]These authors contributed equally to this work
*Correspondence: sikegawa@ims.u-tokyo.ac.jp
http://dx.doi.org/10.1016/j.ajhg.2013.04.003.

Table 1. Clinical and Radiographic Findings of the Individuals with *B3GALT6* Mutations

Subject ID	P1	P2	P3	P4	P5	P6	P7	P8	P9	P10	P11	P12
Family ID	F1	F1	F2	F3	F4	F5	F6	F7	F8	F9	F9	F10
Clinical diagnosis	SEMD-JL1	SEMD-JL1	SEMD-JL1	SEMD-JL1	SEMD-JL1	SEMD-JL1	SEMD-JL1	SEMD-JL1	EDS-PF	EDS-PF	EDS-PF	EDS-PF
General Information												
Ethnicity	Japanese	Japanese	Japanese	Japanese	Japanese	Japanese	Japanese/ Singaporean	Vietnamese	Italian	Italian/ Canadian	Italian/ Canadian	Brazilian
Gender	M	M	F	M	F	F	M	M	M	F	F	F
Age	34 years	31 years	12 years, 7 months	6 years	5 years, 1 month	12 years	2 years, 9 months	34 years	8 months	7 years	1 month	5 years, 1 month
Gestational age	39 weeks, 2 days	full term	37 weeks	40 weeks, 1 day	39 weeks, 5 days	full term	39 weeks	full term	ND	36 weeks	37 weeks	39 weeks
Birth length (cm)	ND	ND	36	ND	43.1	42	43	(average)	ND	44	44	44
Birth weight (g)	ND	2,200	2,124	2,832	2,535	2,222	2,485	3,500	ND	2,097	2,790	3,300
Clinical Features												
Height (cm) (SD)[a]	127.7 (−7.4)	130 (−7.0)	88.8 (−10.7)	94 (−4.0)	90 (−4.0)	118.4 (−5.1)	78.2 (−4.0)	118 (−9.1)	66 (−1.6)	90 (−6.8)	45 (−3.7)	81 (−5.9)
Weight (kg) (SD)[a]	40.3 (−2.2)	36.9 (−2.5)	13.2 (−3.7)	15.4 (−1.5)	14.4 (−1.3)	23.2 (−2.0)	10.6 (−1.9)	28 (−3.3)	5.65 (−3.0)	13.9 (−2.2)	2.65 (−2.8)	8.5 (−8.4)
Craniofacial												
Flat face with prominent forehead	ND	ND	+	+	+	+	+	−	+	+	+	+
Prominent eyes, proptosis	ND	ND	+	−	−	+	+	−	+	+	+	+
Blue sclerae	ND	ND	+	+	+	−	+	−	+	+	+	−
Long upper lip	ND	ND	−	+	+	−	+	+	+	+	+	−
Micrognathia	ND	ND	+	+	+	+	−	+	−	−	−	−
Cleft palate	ND	ND	−	−	−	−	−	−	−	−	−	+
Musculoskeletal												
Kyphoscoliosis[b]	+ (7 months)	+ (1.2 years)	+ (8 months)	+ (infancy)	+ (2 years)	+ (3 months)	+ (8 months)	+ (1 year)	+ (6 months)	++ (prenatal)	++ (prenatal)	++ (2 years)
Spatulate finger	−	ND	+	+	+	+	−	−	+	+	+	−
Finger laxity	ND	ND	+	+	−	−	+	−	++	+	+	+
Large joint laxity	ND	ND	+	+	−	−	+	−	++	++	++	+
Restricted elbow movement	+	ND	+	+	+	−	−	+	+	+	+	+
Hand contracture	−	−	−	−	−	+	−	−	−	+	+	−

(*Continued on next page*)

Table 1. *Continued*

Subject ID	P1	P2	P3	P4	P5	P6	P7	P8	P9	P10	P11	P12
Hip dislocation	–	–	–	+	–	+	–	–	–	+	+	+
Clubfeet	–	–	+	–	–	–	+	–	–	+	+	–
Muscular hypotonia	–	–	+	–	–	–	–	–	++	++	++	++
Skin and Hair												
Doughy skin	ND	ND	+	–	–	–	+	–	++	+	+	+
Hyperextensibility	ND	ND	+	–	–	–	+	–	++	+	+	–
Cutis laxa	ND	ND	–	–	–	–	–	–	+	+	–	+
Sparse hair	ND	ND	–	–	–	–	–	–	+	+	+	–
Others			MR, DD				camptodactyly			DD		pectus excavatum
Radiological Features												
Platyspondyly	+[c]	+[c]	+[c]	+	+	+	+	+	+	+	+	+
Anterior beak of vertebral body[b]	+	+	– (4 years)	– (5 years)	+	+	+	–	+	+	+	+
Short ilia	+	+	+	+	+	+	+	+	+	+	+	+
Prominent lesser trochanter	+	+	+	–	+	+	+	+	+	+	+	+
Metaphyseal flaring	+	+	+	+	+	+	+	+	+	–	+	+
Epiphyseal dysplasia of femoral head	–	–	–	+	–	+	–	–	–	–	+	+
Elbow malalignment	ND	ND	+	+	+	+	+	+	+	+	+	+
Advanced carpal ossification[b]	– (9 years)	ND	– (12 years)	+	+	+	+	ND	+	– (7 years)	–	– (5 years)
Carpal fusion	ND	ND	+	–	–	–	–	–	–	–	–	–
Metacarpal shortening	ND	ND	+	+	+	+	+	+	–	–	+	–
Overtubulation	–	–	–	–	–	–	–	–	+	+	+	+

Abbreviations are as follows: SEMD-JL1, spondyloepimetaphyseal dysplasia with joint laxity type 1; EDS-PF, Ehlers-Danlos syndrome, progeroid form; ND, no data; MR, mitral regurgitation; DD, developmental delay.
[a]At last presentation.
[b]Age at medical attention provided in parentheses.
[c]Absent at age 20 years in P1 and P2 and at age 12 years in P3.

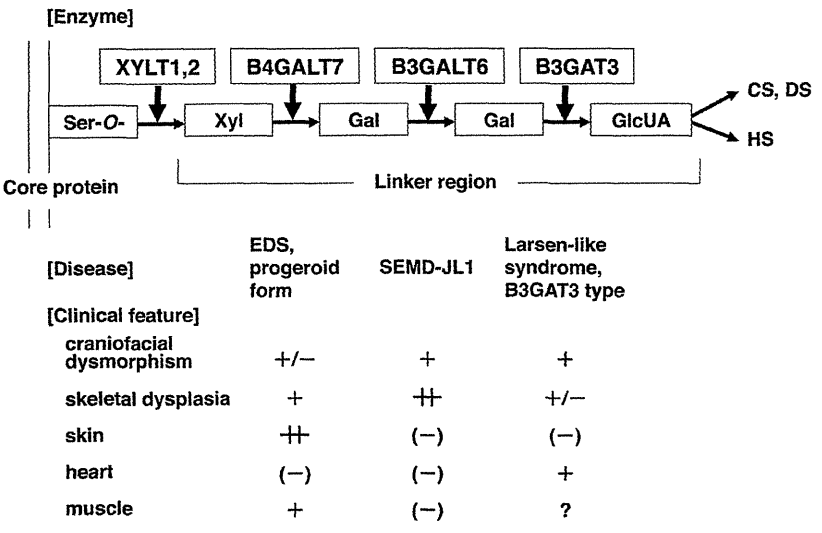

Figure 1. Enzymes Involved in Biosynthesis of the Glycosaminoglycan Linker Region and Summary Features of Diseases Caused by Their Defects Based on a Conventional Concept for the Diseases

The biosyntheses of GAGs start with the formation of a common tetrasaccharide linker sequence covalently attached to the core protein. The linker region synthesis involves a single linear pathway composed of four successive steps catalyzed by distinctive enzymes. Abbreviations are as follows: XYLT, β-xylosyltransferase; B4GALT7, xylosylprotein β1,4-galactosyltransferase, polypeptide 7 (β1,4-galactosyltransferase-I); B3GALT6, UDP-Gal, βGal β1,3-galactosyltransferase polypeptide 6 (β1,3-galactosyltransferase-II); B3GAT3, β-1,3-glucuronyltransferase 3 (glucuronosyltransferase I); Ser-*O*, the serine residue of the GAG attachment site on the proteoglycan core protein; Xyl, xylose; Gal, galactose; GlcUA, D-glucuronic acid; CS, chondroitin sulfate; DS, dermatan sulfate; HS, heparan sulfate; EDS, Ehlers-Danlos syndrome; SEMD-JL1, spondyloepimetaphyseal dysplasia with joint laxity type 1.

from peripheral blood, saliva, or Epstein-Barr virus-immortalized lymphocyte of the individuals with SEMD-JL1 and/or their parents after informed consent. The study was approved by the ethical committee of RIKEN and participating institutions. We captured the exomes of the seven subjects as previously described.[6,7] In brief, we sheared genomic DNA (3 μg) by Covaris S2 system (Covaris) and processed with a SureSelect All Exon V4 kit (Agilent Technologies). We sequenced DNAs captured by the kit with HiSeq 2000 (Illumina) with 101 base pair-end reads. We performed the image analysis and base calling by HiSeq Control Software/Real Time Analysis and CASAVA1.8.2 (Illumina) and mapped the sequences to human genome hg19 by Novoalign. We processed the aligned reads by Picard to remove PCR duplicate. The mean depth of coverage for reads was 132.8×, and, on average, 91.0% of targeted bases had sufficient coverage (20× coverage) and quality for variant calling (Table S1 available online). The variants were called by Genome Analysis Toolkit 1.5-21 (GATK) with the best practice variant detection with the GAKT v.3 and annotated by ANNOVAR (2012 February 23).

Based on the hypothesis that SEMD-JL1 is inherited in an autosomal-recessive fashion, we filtered variants with the script created by BITS (Tokyo, Japan) according to following conditions: (1) variants registered in ESP5400, (2) variants found in our in-house controls (n = 274), (3) synonymous changes, (4) rare variants registered in dbSNP build 135 (MAF < 0.01), and (5) variants associated with segmental duplication. After combining variants selected by the homozygous mutation model and the compound heterozygous mutation model, we selected genes shared by individuals from three or more families. The analysis of the next-generation sequencing identified possible compound heterozygous variants in *B3GALT6* in individuals from three families (Table S2). In addition, two other subjects had possible causal heterozygous variants of *B3GALT6*.

B3GALT6 (RefSeq accession number NM_080605.3) is a single-exon gene on chromosome 1p36.33. It encodes UDP-Gal:βGal β1,3-galactosyltransferase polypeptide 6 (or galactosyltransferase-II: GalT-II), an enzyme involved in the biosynthesis of the glycosaminoglycan (GAG) linker region.[8] The biosyntheses of dermatan sulfate (DS), chondroitin sulfate (CS), and heparin/heparan sulfate (HS) GAGs start with the formation of a tetrasaccharide linker sequence, glucuronic acid-β1-3-galactose-β1-3-galactose-β1-4-xylose-β1 (GlcUA-Gal-Gal-Xyl), which is covalently attached to the core protein. The linker region synthesis involves a single linear pathway composed of four successive steps catalyzed by distinctive enzymes (Figure 1). The first step is the addition of xylose to the hydroxy group of specific serine residues on the core protein by xylosyltransferases from UDP-Xyl, followed by two distinct galactosyltransferases (GalT-I and II) and a glucuronosyltransferase from UDP-Gal and UDP-GlcUA, respectively. The next hexosamine addition is critical because it determines which GAG (i.e., CS, DS, or HS) is assembled on the linker region. GalT-II encoded by *B3GALT6* functions in the third step of the linker formation (Figure 1).

To confirm the results obtained by the next-generation sequencing, we examined the seven subjects used for the next-generation sequencing and an additional subject from a Vietnamese family (F7) by direct sequence of the PCR products from genomic DNAs using 3730xl DNA Analyzer (Applied Biosystems). The Sanger sequencing confirmed all *B3GALT6* mutations found by the next-generation sequencing and identified additional *B3GALT6* mutations. The results indicated that *B3GALT6* mutations were found in all subjects (Tables 2 and S1). All but P4 from F3 were compound heterozygotes of missense mutations. In P4, only a heterozygous c.1A>G (p.Met1?) mutation was found, although we searched for a *B3GALT6* mutation in the entire coding region, 5′ and 3′ UTRs, and flanking

Table 2. *B3GALT6* Mutations in Spondyloepimetaphyseal Dysplasia with Joint Laxity Type 1 and Ehlers-Danlos Syndrome, Progeroid Form

Family	Clinical Diagnosis	Nucleotide Change	Amino Acid Change
F1	SEMD-JL1	c.1A>G	p.Met1?
		c.694C>T	p.Arg232Cys
F2	SEMD-JL1	c.1A>G	p.Met1?
		c.466G>A	p.Asp156Asn
F3[a]	SEMD-JL1	c.1A>G	p.Met1?
F4	SEMD-JL1	c.1A>G	p.Met1?
		c.694C>T	p.Arg232Cys
F5	SEMD-JL1	c.694C>T	p.Arg232Cys
		c.899G>C	p.Cys300Ser
F6	SEMD-JL1	c.1A>G	p.Met1?
		c.193A>G	p.Ser65Gly
F7	SEMD-JL1	c.200C>T	p.Pro67Leu
		c.694C>T	p.Arg232Cys
F8	EDS-PF	c.353delA	p.Asp118Alafs*160
		c.925T>A	p.Ser309Thr
F9	EDS-PF	c.588delG	p.Arg197Alafs*81
		c.925T>A	p.Ser309Thr
F10	EDS-PF	c.16C>T	p.Arg6Trp
		c.415_423del	p.Met139Ala141del

The nucleotide changes are shown with respect to *B3GALT6* mRNA sequence. The corresponding predicted amino acid changes are numbered from the initiating methionine residue.
[a]Only a heterozygous mutation was found.

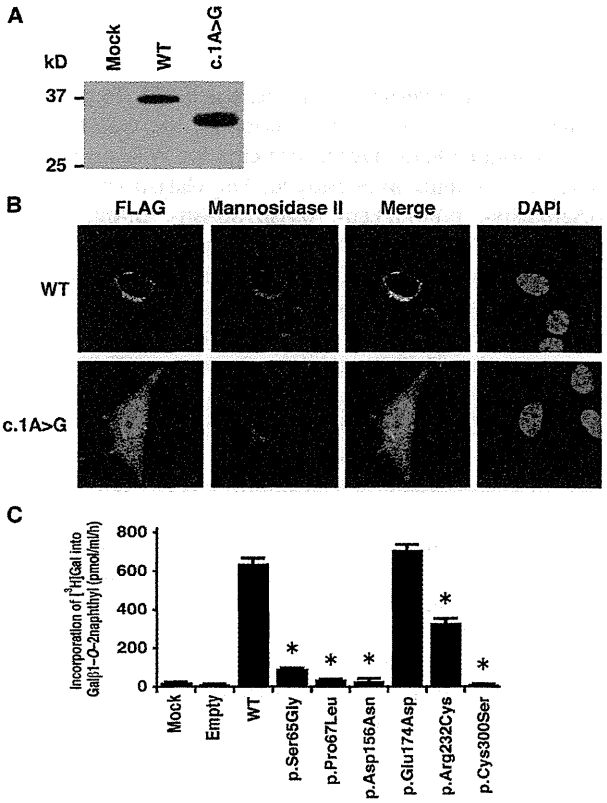

Figure 2. Analyses of B3GALT6 Missense Mutant Proteins Identified in Individuals with SEMD-JL1 In Vitro
(A) Immunoblot analysis of lysates from HeLa cells expressing transfected wild-type (WT) and mutant (c.1A>G) *B3GALT6*. The mutant *B3GALT6* yields a shortened protein. The difference of the molecular sizes between WT and mutant proteins is approximately ~4 kD.
(B) Subcellular localization of B3GALT6. HeLa cells were transfected with WT and mutant (c.1A>G) *B3GALT6*. Cells were stained with anti-FLAG (green), anti-α-mannosidase II (red), and 4′,6-diamidino-2-phenylindole (DAPI; blue). WT was expressed in the Golgi, but the mutant was found in cytoplasm and nucleus.
(C) Decreased enzyme activities of the missense mutant proteins (p.Ser65Gly, p.Pro67Lys, p.Asp156Asn, p.Arg232Cys, and p.Cys300Ser). p.Glu174Asp is a common polymorphism in the public database. The GalT-II activity is measured by incorporation of [^{3}H]Gal into Galβ1-*O*-2naphthyl (*p*mol/ml/hr) and represents the averages of three independent experiments performed in triplicate. Empty and mock indicate the GalT-II activity obtained with the conditioned medium transfected with or without an empty vector. *$p < 0.0001$ versus WT (one-way analysis of variance with Dunnett's adjustment).

regions of *B3GALT6*. Most of the mutations are predicted to be disease causing by in silico analysis. The c.1A>G (p.Met1?) mutation was found in individuals from five of the seven families.

Although mutations affecting initiation codons have been reported to be pathogenic in several diseases,[9] the effects of initiation codon mutations on the encoded protein are variable among the genes. We therefore investigated the effect of the c.1A>G (p.Met1?) mutation on the protein by using C-terminally FLAG-tagged B3GALT6 with and without the mutation expressed in HeLa cells (RIKEN Cell Bank). We detected the mutant B3GALT6 protein with a molecular weight ~4 kD lower compared with the wild-type (WT) protein (Figure 2A). These results suggest that translation initiation at the second ATG of the coding sequence, at position c.124, would become the initiation codon because of the mutation, probably resulting in an N-terminal deletion of 41 amino acids (p.Met1_Ala41del), in the same open reading frame that contains the transmembrane domain. We then examined the subcellular localization of the mutant B3GALT6 protein by immunocytochemistry. The immunofluorescence for WT-B3GALT6 was observed in a perinuclear region overlapping with that for α-mannosidase II, a marker of the Golgi as previously reported.[8] In contrast, the immunofluorescence for the mutant B3GALT6 protein was observed in the nucleus and cytoplasm (Figure 2B). Therefore, the mutant protein can be considered to be functionally null because of the mislocalization.

To investigate the causality of other *B3GALT6* missense mutations, we also examined the subcellular localization of the mutant B3GALT6 proteins by immunocytochemistry. c.193A>G (p.Ser65Gly), c.200C>T (p.Pro67Leu),